Journal Pre-proof

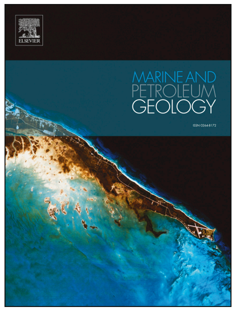

Interactions between sediment production and transport in the geometry of carbonate platforms: Insights from forward modeling of the great bank of Guizhou (early to Middle Triassic), south China

Xiaowei Li, Oriol Falivene, Marcello Minzoni, Daniel J. Lehrmann, John J.G. Reijmer, Michele Morsilli, Khalid A.H. Al-Ramadan, Meiyi Yu, Jonathan L. Payne

PII: S0264-8172(20)30199-9

DOI: https://doi.org/10.1016/j.marpetgeo.2020.104416

Reference: JMPG 104416

To appear in: *Marine and Petroleum Geology*

Received Date: 3 December 2019

Revised Date: 21 April 2020

Accepted Date: 22 April 2020

Please cite this article as: Li, X., Falivene, O., Minzoni, M., Lehrmann, D.J., Reijmer, J.J.G., Morsilli, M., Al-Ramadan, K.A.H., Yu, M., Payne, J.L., Interactions between sediment production and transport in the geometry of carbonate platforms: Insights from forward modeling of the great bank of Guizhou (early to Middle Triassic), south China, *Marine and Petroleum Geology* (2020), doi: https://doi.org/10.1016/j.marpetgeo.2020.104416.

All authors' individual contributions are followed:

Authors	Contributions
Xiaowei Li	Conceptualization, writing-reviewing and editing, methodology, funding acquisition, formal analysis, visualization
Oriol Falivene	writing-reviewing and editing, methodology
Marcello Minzoni	writing-reviewing and editing, methodology
Daniel J. Lehrmann	Conceptualization, writing-reviewing and editing, funding acquisition, visualization
John J. G. Reijmer	writing-reviewing and editing
Michele Morsilli	writing-reviewing and editing
Khalid A. H. Al-Ramadan	writing-reviewing and editing
Meiyi Yu	writing-reviewing and editing
Jonathan L. Payne	Conceptualization, methodology, writing-reviewing and editing, funding acquisition

Article type: Research paper to *Marine and Petroleum Geology*

Interactions between sediment production and transport in the geometry of carbonate platforms: Insights from forward modeling of the Great Bank of Guizhou (Early to Middle Triassic), south China

Xiaowei Li[1*], Oriol Falivene[2], Marcello Minzoni[3,8], Daniel J. Lehrmann[4], John J. G. Reijmer[5], Michele Morsilli[6], Khalid A. H. Al-Ramadan[5], Meiyi Yu[7], Jonathan L. Payne[1]

[1*] Department of Geological Sciences, Stanford University, Stanford, CA 94305, USA, xwli@stanford.edu; geo.xwli@gmail.com

[2] Shell Westhollow Technology Center, 3333 Highway 6 S, Houston, TX 77082, USA

[3] Shell Exploration and Production Company, 150 N Dairy Ashford Road, Houston, TX 77079, USA

[4] Department of Geosciences, Trinity University, San Antonio, TX 78212, USA

[5] College of Petroleum Engineering & Geosciences, King Fahd University of Petroleum & Minerals, Dhahran, 31261, Saudi Arabia

[6] Dipartimento di Fisica e Scienze della Terra, Università di Ferrara, Via G. Saragat 1, 44122 Ferrara, Italy

[7] Department of Resources and Environmental Engineering, Guizhou University, Guiyang, Guizhou 550025, China

[8] Current address: Department of Geological Sciences, University of Alabama, Tuscaloosa, AL 35487, USA

ABSTRACT

Carbonate platforms grow through the precipitation, transport, and final deposition of carbonate sediment out of seawater. Quantifying the relative contributions of initial production versus subsequent transport in determining the growth rates and geometries of platforms remains a significant challenge. In this study, stratigraphic forward modeling is used to quantify the roles of sediment production, transport, and deposition during each growth stage of a Permian-Triassic carbonate platform with a complex growth history. Parameter optimization and sensitivity analysis show that, within the range of reasonable tested values, the morphology of the platform is most sensitive to sediment transport, moderately sensitive to maximum carbonate production rate, and least sensitive to the productivity-depth curve. The ramp-to-high relief, steep-sloped platform transition during Early Triassic time can be explained by any factor that limits sediment transport from shallow water areas of high production to the slope and basin. Reefs may play a role in limiting sediment transport on many platforms but other processes, such as early marine cementation, or carbonate production along the slope, may be equally capable of yielding this shift in platform geometry. In this particular case, early lithification of ooid and skeletal shoals on the platform margin, perhaps facilitated by unusually high carbonate saturation state of seawater, may have inhibited sediment transport into the basin prior to the development of a reef on the platform margin. Later, Anisian progradation of the platform margin can be explained by the development of a slope factory rather than requiring increased sediment transport from the platform top. The development of an escarpment margin in the Ladinian is mainly influenced by accommodation in the slope profile created by antecedent topography. A general implication from the model results is that the growth of steep-sloped carbonate platforms lacking slope microbial factory may often be limited by transport of sediment from the platform top to accommodation on the slope rather than by the intrinsic production capacity of the platform top factory.

Keywords: carbonate platform; geometry; sediment production; transport; carbonate saturation; carbonate factory

1. INTRODUCTION

Carbonate platform architecture is influenced by the interplay of physical, chemical, and biological factors that cause complex variations in platform morphology (e.g., ramp, steep-sloped platform, or bypass escarpment) and internal facies distribution (Bergmann et al., 2013; Halfar et al., 2004; Higgins et al., 2009; Lukasik and Simo, 2008; Verwer et al., 2013). One important approach to assessing the influences of physical, chemical, and biological processes on carbonate platform development has been the analysis of modern and ancient systems through outcrop or subsurface stratigraphic methods and on-site oceanographic measurements (Harris et al., 2015; Lehrmann et al., 1998; Lukasik and Simo, 2008; Purkis et al., 2015; Reeder and Rankey, 2008; Reijmer et al., 2009; Swart et al., 2009; Verwer et al., 2013). A complementary approach is the application of numerical stratigraphic forward modeling. To date, stratigraphic forward modeling has been applied to carbonate systems in order to (1) test component sedimentary patterns, such as sedimentary cyclicity (Spencer and Demicco, 1989) and the origin and distribution of hiatuses (Burgess and Wright, 2003); (2) create conceptual models of platform geometry and internal architecture (Bosence and Waltham, 1990; Busson et al., 2019; Williams et al., 2011); and (3) predict sediment distribution and reservoir architecture for hydrocarbon applications (Bassant and Harris, 2008; Gervais et al., 2018; Liechoscki de Paula Faria et al., 2017; Warrlich et al., 2008). Most of the carbonate platforms that have been simulated by stratigraphic forward modeling display a single stacking pattern throughout their entire growth history [e.g., aggradation (Barrett and Webster, 2017), progradation (Berra et al., 2016; Castell et al., 2007; Saura et al., 2013), retrogradation and drowning (Seard et al., 2013; Warrlich et al., 2002)] and one morphotype [e.g., ramp or steep-sloped platform (Berra et al., 2016; Busson et al., 2019; Castell et al., 2007; Kolodka et al., 2015; Liechoscki de Paula Faria et al., 2017; Richet et al., 2011; Warrlich et al., 2008)]. Previous studies have modeled the roles of various factors on carbonate platform evolution such as subsidence rates, sediment production rates, sea-level fluctuation, and sediment redistribution (Warrlich et al., 2002; Williams et al., 2011). However, a significant challenge remains to quantitatively assess which processes play dominant roles and interact to govern large changes in platform morphology through time.

The Great Bank of Guizhou (GBG), an isolated carbonate platform of Permian-Triassic age in the Nanpanjiang Basin of south China (Figs. 1 and 2), is an ideal test case for assessing and quantifying causes of variation in platform morphology across time (Kelley et al., 2020; Li et al., 2012; Minzoni et al., 2013). The stratigraphic architecture of the GBG, from its inception to its demise, is exceptionally well exposed along intact platform-to-basin transects such as the Bianyang syncline (Fig. 3). In addition, its lithostratigraphy, biostratigraphy, and chemostratigraphy have been well established for correlation from platform to basin (Kelley et al., 2020; Lehrmann et al., 2015b, 1998; Meyer et al., 2011; Payne et al., 2004).

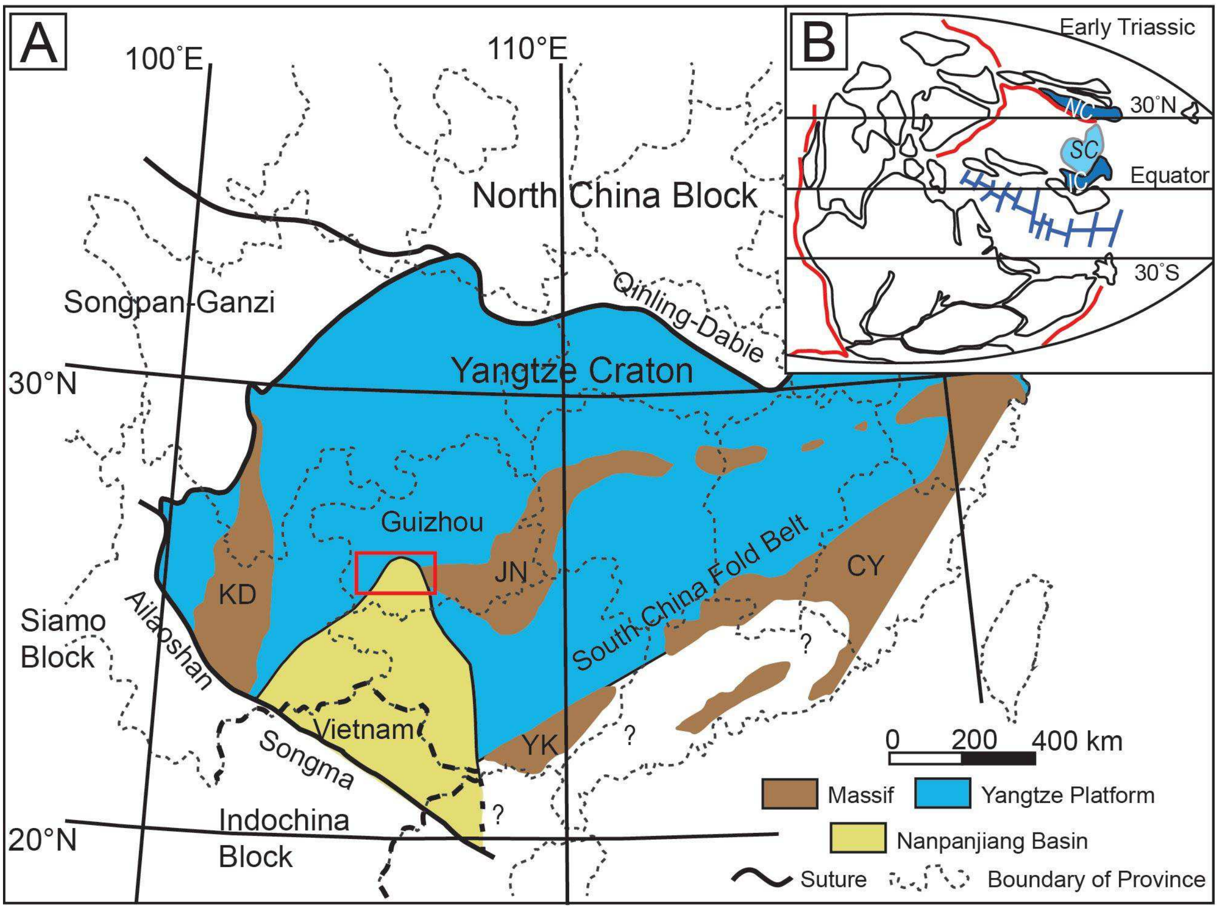

Figure 1. Tectonic map of south China block. (A) Location of the Nanpanjiang Basin and Precambrian massifs that border the basin and potentially provide terrigenous sediments into the Nanpanjiang Basin: Khamdian (KD), Jiangnan (JN), Yunkai (YK), and Cathaysian (CY). South China block comprises the Yangtze craton and south China fold belt. A red box denotes the area shown in Figure 2A. (B) Global plate reconstruction and locations of south China block (SC), north China block (NC), and IndoChina block (IC) in Early Triassic time. Modified after Minzoni et al. (2013).

The GBG experienced substantial changes in morphology across its accumulation history. The platform initiated as a low-relief ramp during latest Permian time. It continued to accumulate as a ramp with ooid shoals during earliest Triassic time but then developed a steep-sloped platform morphology with significant relief above the adjacent basin during the Early Triassic (Kelley et al., 2020, 2017). The platform evolved into a high-relief, prograding platform geometry with a reef on the margin and slope during Middle Triassic (Anisian) time before developing a bypass escarpment morphology in the northern margin and a collapsed escarpment in the southern margin later in the Middle Triassic (Ladinian) prior to drowning early in the Carnian (Fig. 3; Kelley et al., 2020; Lehrmann et al., 2020, 1998; Li et al., 2012). The transitions in platform geometry were accompanied by distinctive changes at the platform margin and along the slope from a tropical to a microbial factory. Consequently, the GBG offers an unusual opportunity to test if and how transitions in carbonate factory types contributed to coeval shifts in platform architecture (Pomar, 2001).

In order to advance understanding of the dominant variables governing the evolution of platform morphology (ramp, steep-sloped platform, bypass escarpment, etc.), it is necessary to model facies architecture at the scale of exceptional outcrop or seismic-scale subsurface analogues rather than attempting to model the small-scale facies and microfacies distributions. By exploring the parameter combinations required to mimic the evolution of the platform morphology of the GBG along the platform-to-basin transect of the Bianyang syncline through stratigraphic forward modeling, the goals of this study are: (1) to quantify the factors that enabled the ramp to steep-sloped platform geometric transition in the Early Triassic in the absence of a microbial or metazoan reef framework at the platform margin and without synsedimentary tectonic modification of the margin; and (2) to assess sensitivity of overall platform morphology of the GBG to patterns of sediment production and transport that is generally most poorly constrained or non-explicitly introduced in previous modeling studies (e.g., Kolodka et al., 2015; Liechoscki de Paula Faria et al., 2017; Saura et al., 2013) within the constraints of local subsidence, global sea-level fluctuation, and geologic setting.

2. GEOLOGIC SETTING

The Nanpanjiang Basin formed an embayment to the south (current coordinates) of an attached carbonate platform, the Yangtze Platform (Fig. 1). During the latest Permian, a local marine transgression forced the south-facing Changhsingian Yangtze Platform margin to backstep approximately 100 km, from near the present city of Luodian to the Guiyang area (Fig. 2). Antecedent topography inherited from a Late Permian shelf-margin reef complex along the former Changhsingian Yangtze Platform margin and a series of patch reefs in the former platform interior (Fig. 2B) served as nuclei for the growth of an isolated carbonate platform, the GBG (Fig. 3; Lehrmann et al., 1998; Li et al., 2012).

The western sector of the GBG is dissected by the N-S-trending faulted Bianyang syncline (Fig. 2C) that exposes a continuous 2-D platform-to-basin cross-section of the architecture and preserved bathymetric profile through the platform and its northern and southern flanks (Fig. 3). Strata of the cross-section dip at approximately 65° to the southwest (Fig. 3A). Details of the facies composition, texture and sedimentary structures of the GBG are documented in detail in previous studies (Kelley et al., 2020; Lehrmann et al., 2007, 1998; Li et al., 2012; Minzoni et al., 2013).

Here, the overall platform evolution of the GBG is summarized with a focus on the evolution of the platform morphology and facies architecture. Following initiation on antecedent topography inherited from the Late Permian (Figs. 2B and 3B), the GBG developed a ramp morphology with ooid shoals in the earliest of the Induan. The GBG evolved into a steep-sloped, high-relief platform with ooid shoals at the margin by the Olenekian of the Early Triassic (Figs. 3B and 4; Kelley et al., 2020). During the Anisian, the GBG developed a steep, prograding morphology with margin and slope composed of *Tubiphytes* boundstone (Kelley et al., 2020). In-situ *Tubiphytes* boundstone grew on the upper two-thirds of the slope. In the Ladinian the platform locked into an aggradational mode, developing a high-relief bypass escarpment morphology on the north flank, and a collapsed margin that includes a steep convex-bankward embayment on the south flank (Lehrmann et al., 2020). The GBG was drowned and buried with siliciclastic turbidites in the Carnian (Fig. 3; Lehrmann et al., 2007, 1998).

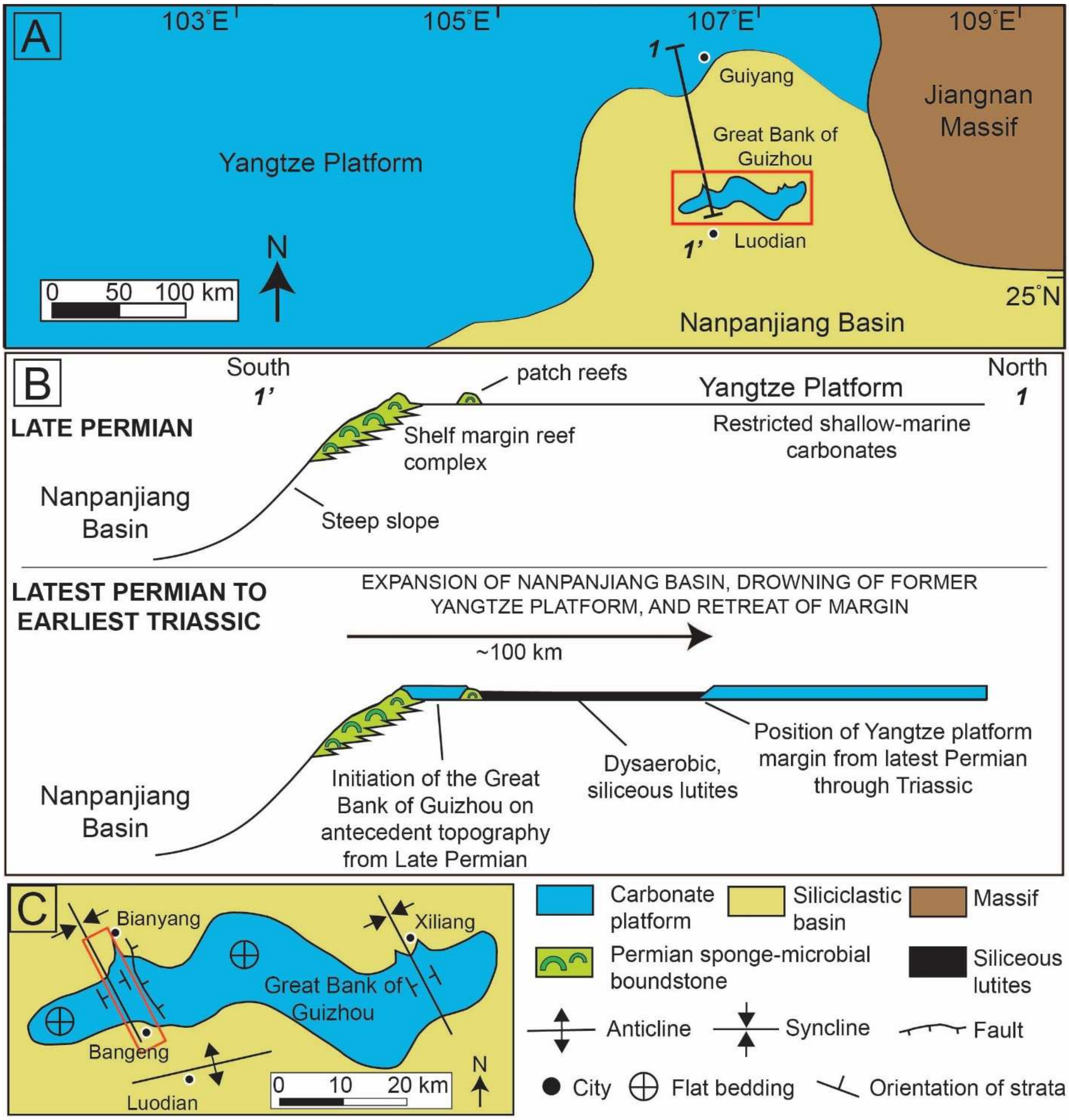

Figure 2. Detailed view of the Nanpanjiang Basin and the Great Bank Guizhou (GBG). (A) Position of the GBG is indicated by a red box. Cross section (1-1') is shown in (B). (B) Schematic cross sections illustrating latest Permian drowning of the Yangtze Platform and initial accumulation of the GBG on antecedent topography inherited from the Late Permian (modified after Lehrmann et al., 1998). (C) Detailed view of the GBG with the Bianyang syncline (faulted syncline) that exposes a platform-to-basin transect which is enclosed in a red box. The red box in (C) denotes the studied transect of the GBG whose satellite image and stratigraphic architecture are shown in Figure 3.

The earliest deposits of the GBG were composed of sponge-microbial boundstone and open-marine skeletal packstone-grainstone composed of a high biodiversity, open-marine biota that nucleated on top the antecedent topography inherited from the Upper Permian (Figs. 2B and 3B; Lehrmann et al., 1998; Li et al., 2012). Upon initiation, the platform had some relief, likely a few hundred meters, above the pre-existing Nanpanjiang Basin to the south but quite limited relief, likely tens of meters, above the drowned Yangtze Platform to the north (Fig. 3B).

In the beginning of the Induan, the GBG had a ramp profile with ooid shoals at the margin (the slope angle is ~1.5° in Fig. 3B; Lehrmann et al., 1998). The GBG developed an aggradational accretionary margin stabilized by early marine cements with progressively steepening slopes during the Induan (Kelley et al., 2020). By the end of the Induan, approximately 1.5 Myr after the Permian/Triassic transition, the GBG had evolved into a high-relief, steep-sloped (17° to 21°) platform where the northern margin stood approximately 300 m above the adjacent basin (Fig. 3; Kelley et al., 2020). Facies in the platform interior change upward from microbial boundstone to thin-bedded lime mudstone, to dolomitized oolite, and next to peritidal thrombolite-bearing cyclic limestone (Figs. 3 and 5), representing shallow subtidal to peritidal environments. A low diversity fauna dominated by gastropods and bivalves in the platform interior suggests a restricted environment, likely due to the presence of shoals at the margin. Marginal shoal facies, approximately 0.3 to 0.4 km wide, comprise oolitic grainstone with subordinate molluscan packstone (Lehrmann et al., 1998; Rongling section in Figs. 3B and 5). Coeval slope facies are composed of shale, punctuated by an upward-increasing occurrence of carbonate debris-flow breccia, carbonate turbidites, and lime mudstone (Figs. 3B and 5). Carbonate debris flows and carbonate turbidites contain oolite clasts, ooids and bivalve fragments primarily sourced from oolitic shoals at the platform margin (Lehrmann et al., 1998; Fig. 5). Lime mudstone along the slope resulted from export of lime mud from the platform margin and interior to the slope as periplatform ooze.

The aggradational accretionary margin was stabilized by early marine cement during the Olenekian, generating a high-relief (~900 m) carbonate platform with a steep slope (Kelley et al., 2020). Oolitic shoals continued to dominate at the platform margin (Rongling section in Figs. 3 and 5), whereas the platform interior consists of dolomitized peritidal facies (Figs. 3 and 5; Lehrmann et al., 1998; Kelley et al., 2020). Steep slope facies (23° to 31°) continue to be composed of carbonate debris-flow breccia, carbonate turbidites containing oolite clasts, ooids and bivalve fragments and periplatform lime mudstone sourced from the margin and interior (Fig. 5; Kelley et al., 2020).

The northern margin of the GBG at Bianyang developed a steep-sloped (23° to 27°) prograding morphology during Anisian time (Fig. 3B; Kelley et al., 2020). Slope deposits are mainly composed of *Tubiphytes* boundstone with abundant early marine cements, boundstone-derived breccia, and lime mudstone, packstone, and grainstone. *Tubiphytes* boundstone dominates the platform margin and upper two-thirds of the slope (Fig. 3B) whereas boundstone-derived debris-flow breccia, carbonate turbidite packstone-grainstone and peri-platform pelagic lime mudstone dominate in the lower slope and extend to the basin margin along with subordinate *Tubiphytes* boundstone (Lehrmann et al., 1998; Kelley et al., 2020). The Anisian slope deposits of the GBG contain a large proportion (~60%) of in-situ *Tubiphytes* boundstone indicating that carbonate production on the slope promoted progradation of the platform, analogous to Middle Triassic slope facies in the Sella (Keim and Schlager, 2001) and Latemar (Marangon et al., 2011) carbonate platforms. As the northern margin of the GBG prograded, the interior deposited peritidal cyclic carbonate composed of meter-scale, shoaling upward cycles with burrowed, molluscan-peloidal packstone at the base and fenestral laminate caps (Fig. 5). *Tubiphytes* boundstone also formed at the southern margin during this time; however, the architecture is unknown because of collapse and truncation of the margin during the Ladinian (Fig. 3B; Li et al., 2012; Lehrmann et al., 2020).

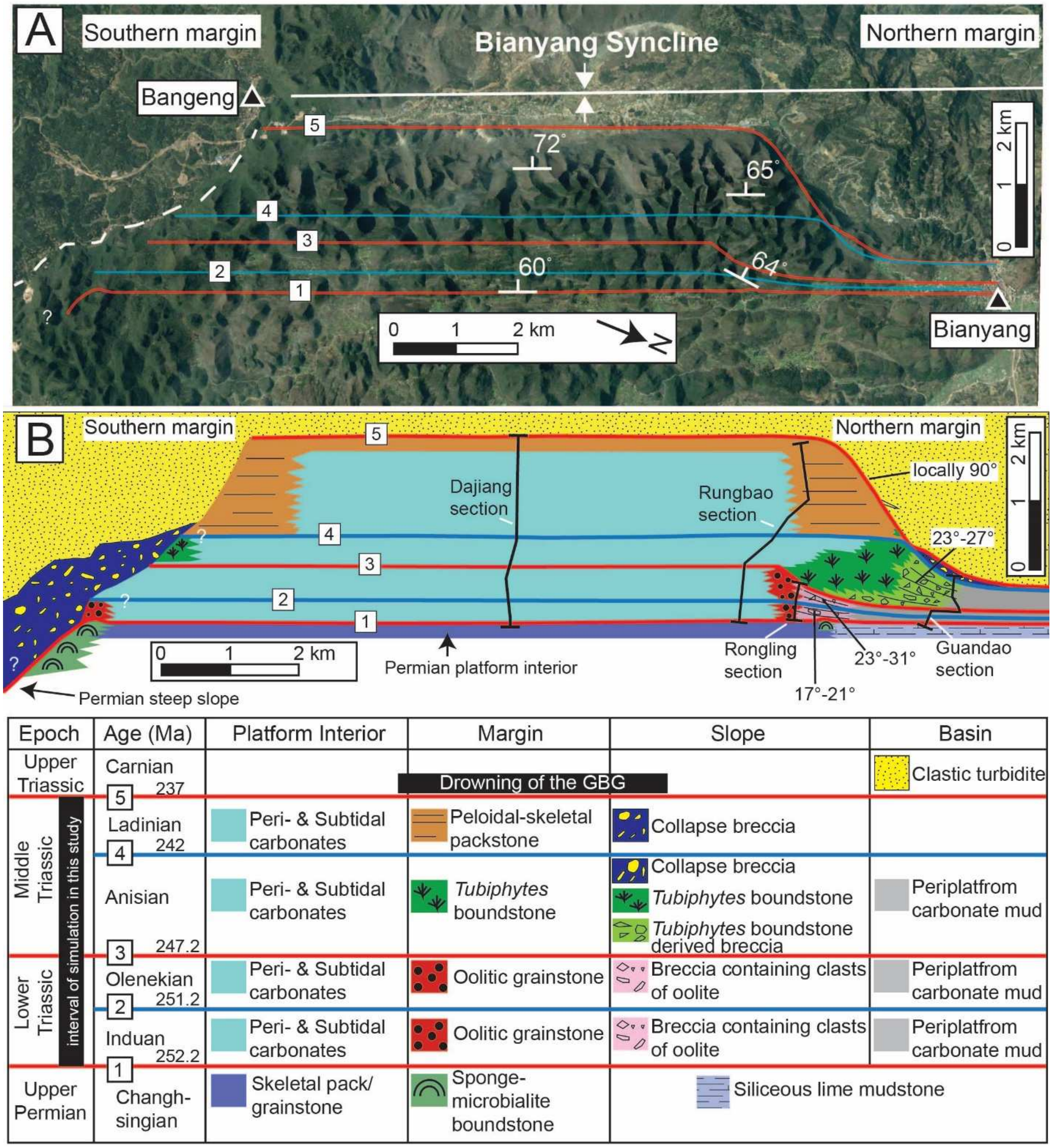

Figure 3. Satellite image and stratigraphic architecture of the GBG along the Bianyang syncline (A) Satellite image of the GBG. The GBG stands out in the satellite image because of the difference in topography of the karsted carbonates of the platform and the stream-eroded siliciclastics in the basin. Dashed white curve defines the outline of scalloped southern margin near Bangeng. Courtesy of GoogleEarth. (B) Platform architecture and principal lithofacies of the GBG through time. The architecture of the northern margin comes from Lehrmann et al. (1998) and Kelley et al. (2020). The architecture within the platform interior is from Lehrmann et al. (1998). The southern margin architecture originates from Lehrmann et al. (2020). Detailed facies features and description are reported in Lehrmann et al. (1998 and 2020) and Kelley et al. (2020). For interpretation of the references to color in this figure legend, the reader is referred to the web version of this article.

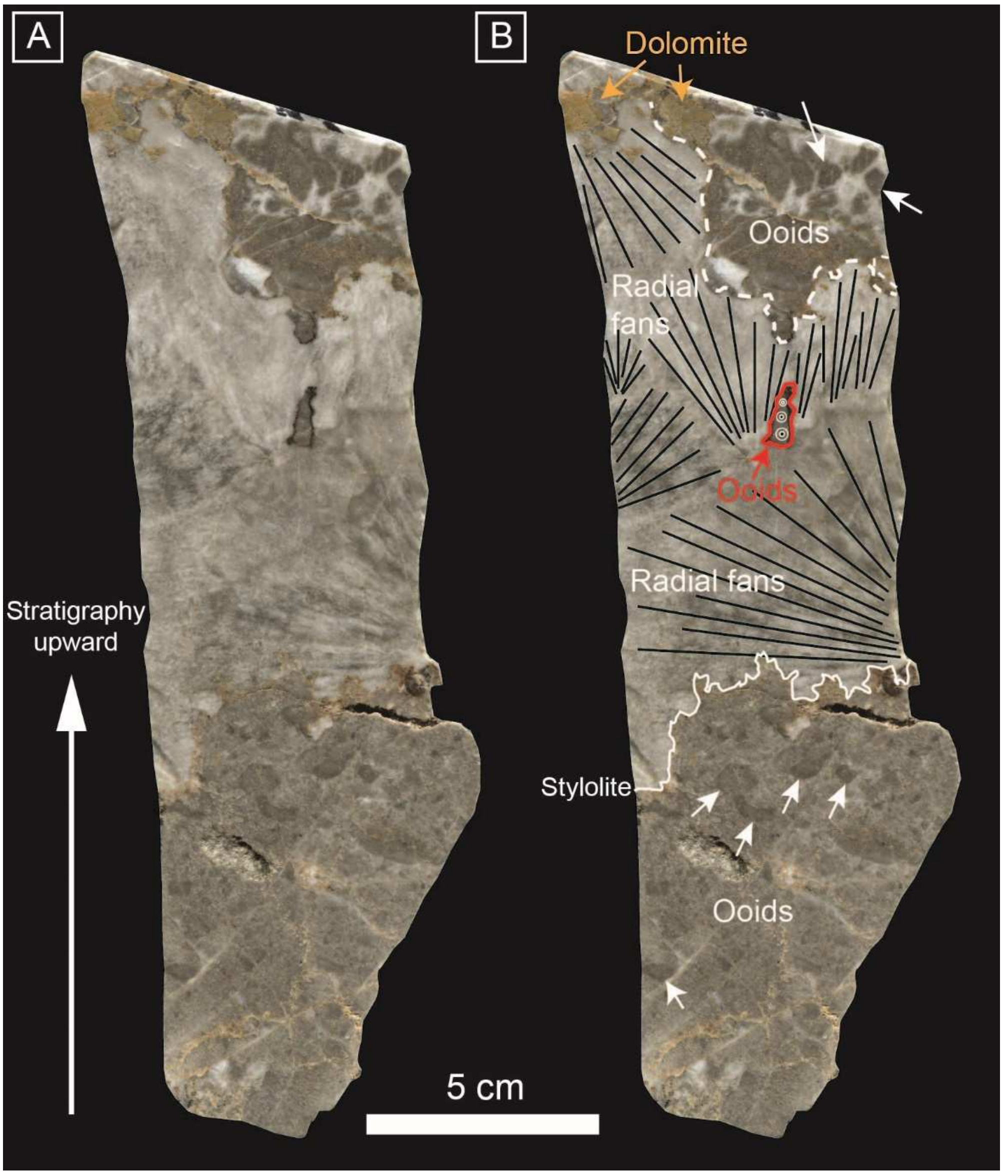

Figure 4. A polished slab of Lower Triassic oolite from Rongling section at the northern margin of the GBG. (A) The slab without annotation. (B) The same slab with annotation. Note several generations of radial carbonate fans stack upon each other. The radial carbonate fans possibly grew on the seafloor (Woods et al., 1999) or were likely preserved within sheet cracks in oolite. Coated composite grains that contain multiple ooids are pointed by white arrows. See Figures 3 and 5 for more details about Rongling section.

During the Ladinian, the northern margin of the GBG developed a high-relief bypass escarpment morphology while the southern margin was truncated by catastrophic collapse (Fig. 3B; Lehrmann et al., 1998 and 2020; Li et al., 2012; Minzoni et al., 2013). Facies along the northern escarpment margin mainly contain skeletal-peloidal packstone-grainstone shoals with local *Tubiphytes*-sponge-coral patch reefs (Lehrmann et al., 1998). Lehrmann et al. (1998) noted that breccia debris at the foot of the northern escarpment contains clasts composed of *Tubiphytes*-sponge-coral boundstone indicating erosion from the escarpment; however, the relatively small volume of the debris at the foot of the northern escarpment shows that the shedding was not extensive. In contrast, the southern margin at Bangeng shows a concave-up geometry recognizable in satellite images (Fig. 3A) that is interpreted to result from margin failure and collapse (Lehrmann et al., 2020; Li et al., 2012). Collapse truncated the Lower Triassic through Ladinian facies along the escarpment, and slope breccia contains clasts eroded from the collapsed margin (Fig. 3; Li et al., 2012; Lehrmann et al., 2020). During the Ladinian, the platform interior developed an initial atoll-like morphology with subtidal molluscan-oncolitic packstone in the central lagoon grading laterally and seaward to peritidal limestone closer to the platform margins (Figs. 3B and 5; Lehrmann et al., 1998). Later in the Ladinian, peritidal limestone extended across the entire platform, yielding a flat-topped profile (Figs. 3B and 5; Lehrmann et al., 1998).

Near the end of the Ladinian, a shift to subtidal facies indicates a deepening event in the platform interior (Lehrmann et al., 1998), followed by drowning of the platform in the beginning of the Late Triassic (Carnian) due to accelerated subsidence (Lehrmann et al., 2007, 1998). The drowning event is reflected by an upward shift to dark grey, nodular, argillaceous oncolitic wackestone containing deep-marine Neogondolellid conodonts followed by burial of the platform by siliciclastic mudrock (Lehrmann et al., 1998 and 2007; Fig. 5). Subsequently, the GBG was buried by a thick succession of siliciclastic turbidites in the Carnian (Lehrmann et al., 2015a, 2007, 1998).

3. MODELING PROCESSES AND CONSTRAINTS

The GBG was used as a reference platform for the construction of stratigraphic forward models exploring the combinations of parameter values compatible with the observed platform evolution. Numerical models were constructed using the DIONISOS software (Granjeon and Joseph, 1999) on an 80 km-long by 2 km-wide transect, using an initial topography equivalent to that of the 2-D cross-section exposed along the Bianyang syncline (Figs. 2B and 3). Because (1) the GBG has a long growth history (252.2 – 237 Ma), (2) its area of simulation is 160 km^2, and (3) this study mainly aims to investigate sensitivity of platform morphology, rather than detailed stratigraphic architecture and internal facies distribution, to different controls, the models were built at a spatial resolution of 0.5 km and temporal resolution of 25,000 yr with a reasonably acceptable computational duration of running models (~1.7 hours per model), spanning from 252.2 to 237 Ma (ICS, 2013). In addition, the average duration of a single peritidal cycle on the platform interior of the GBG is less than 22,000 yr (Yang and Lehrmann, 2003); therefore, the temporal resolution is not capable of reflecting such detail as peritidal cycles and their variations in space and time.

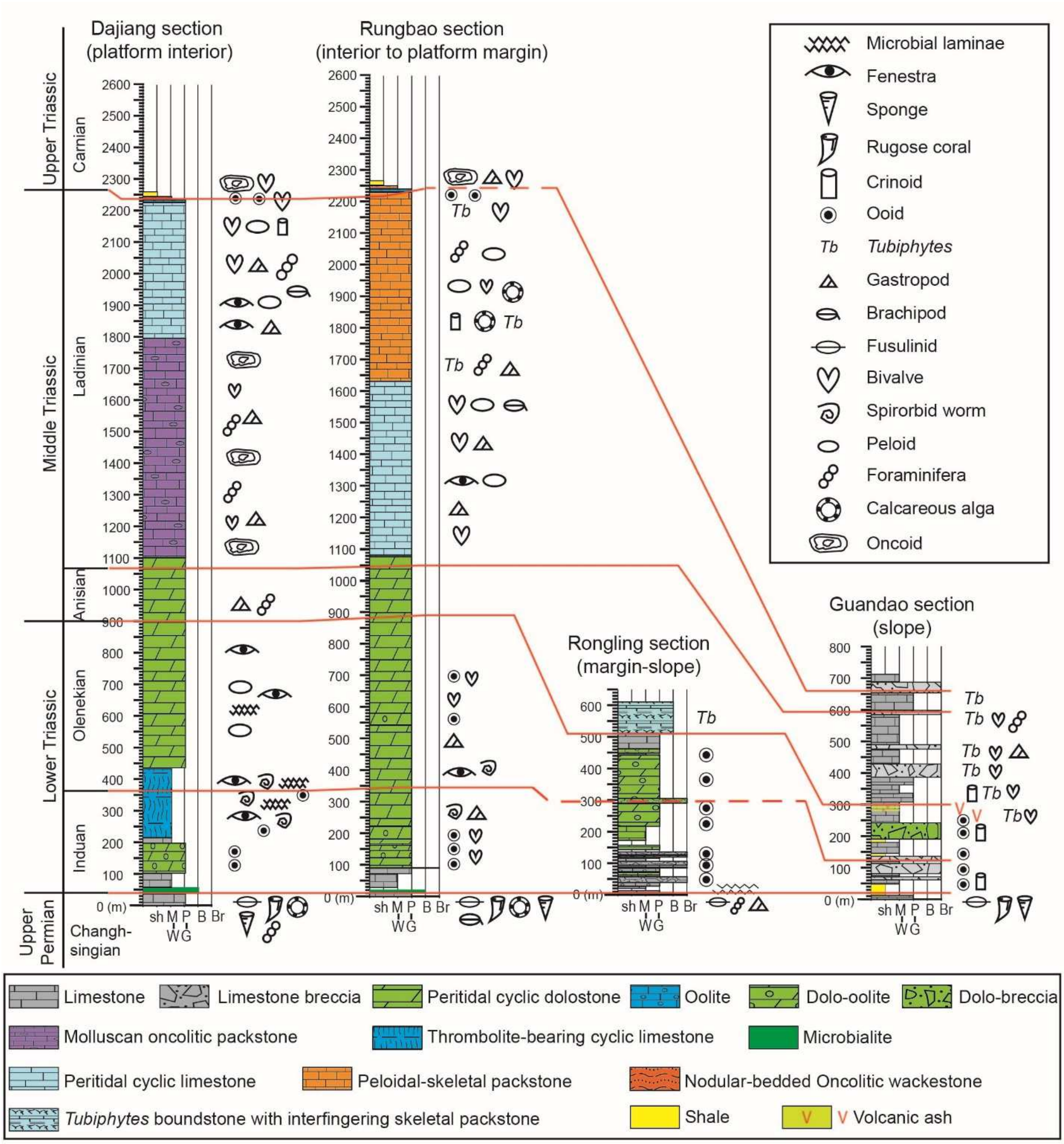

Figure 5. Correlation of measured stratigraphic sections across the platform-to-basin transition based on carbon isotope chemostratigraphy (red lines) modified from Lehrmann et al. (2015b) and Kelley et al. (2020). Ages are based on conodont biostratigraphy at Guandao section (Lehrmann et al., 2015b). See the locations of stratigraphic sections in Figure 3B. Abbreviation: sh = shale, M-W = mudstone and wackestone, P-G = packstone and grainstone, B = boundstone, Br = breccia.

3.1 Accommodation

The initial topography (latest Permian) of the GBG was mainly controlled by the antecedent topography of the shelf-margin reef complex near the former Permian platform margin and associated patch reefs to the north (Figs. 2B and 3; Lehrmann et al., 1998; Li et al., 2012). In the model, the initial bathymetry of the platform interior was assumed as 10 meters below sea level based on the diverse biota including calcareous algae, fragmented fossils, and grainstone texture of the uppermost Permian rocks indicating an open-marine, shallow-subtidal, moderately agitated environment (Lehrmann et al., 1998).

The initial topography for model runs was based on field constraints on the antecedent topography inherited from the Upper Permian where the margin reef complex and associated patch reefs generally confine the initial nucleation location of the GBG (Figs. 6 and 7A). In the south, the shelf-margin reef complex faced the deeper waters of the central Nanpanjiang Basin (Figs. 2B and 7A). A water depth of 250 m and a clinoform slope angle of 35° were used to approximate the initial topography of the southern margin (Fig. 7A). Moving northward to the former Permian platform interior, the assumed water depth near the patch reefs increases from 2 m to 30 m below sea level across 2500 m laterally (Fig. 7A). Perched above the Upper Permian margin, the GBG is inferred to have developed with approximately 10 m elevation above the substrate, with change across a lateral distance of 500 m on the south and north edges of the platform (Fig. 7A).

In DIONISOS, simulation of accommodation during each time step includes the effects of sediment compaction/dissolution, eustatic sea level change, local subsidence, and sediment erosion (Fig. 6; Granjeon and Joseph, 1999). In the model runs, the thicknesses from measured stratigraphic sections were used without correction for differential compaction and dissolution as the data for comparison because existing data do not allow precise correction for these effects. Furthermore, early marine cementation filled a large portion of the depositional porosity, stabilizing the Early Triassic and Middle Triassic platform margin and limiting the effect of compaction on the overall platform architecture (Kelley et al., 2020; Lehrmann et al., 2012; Payne et al., 2006).

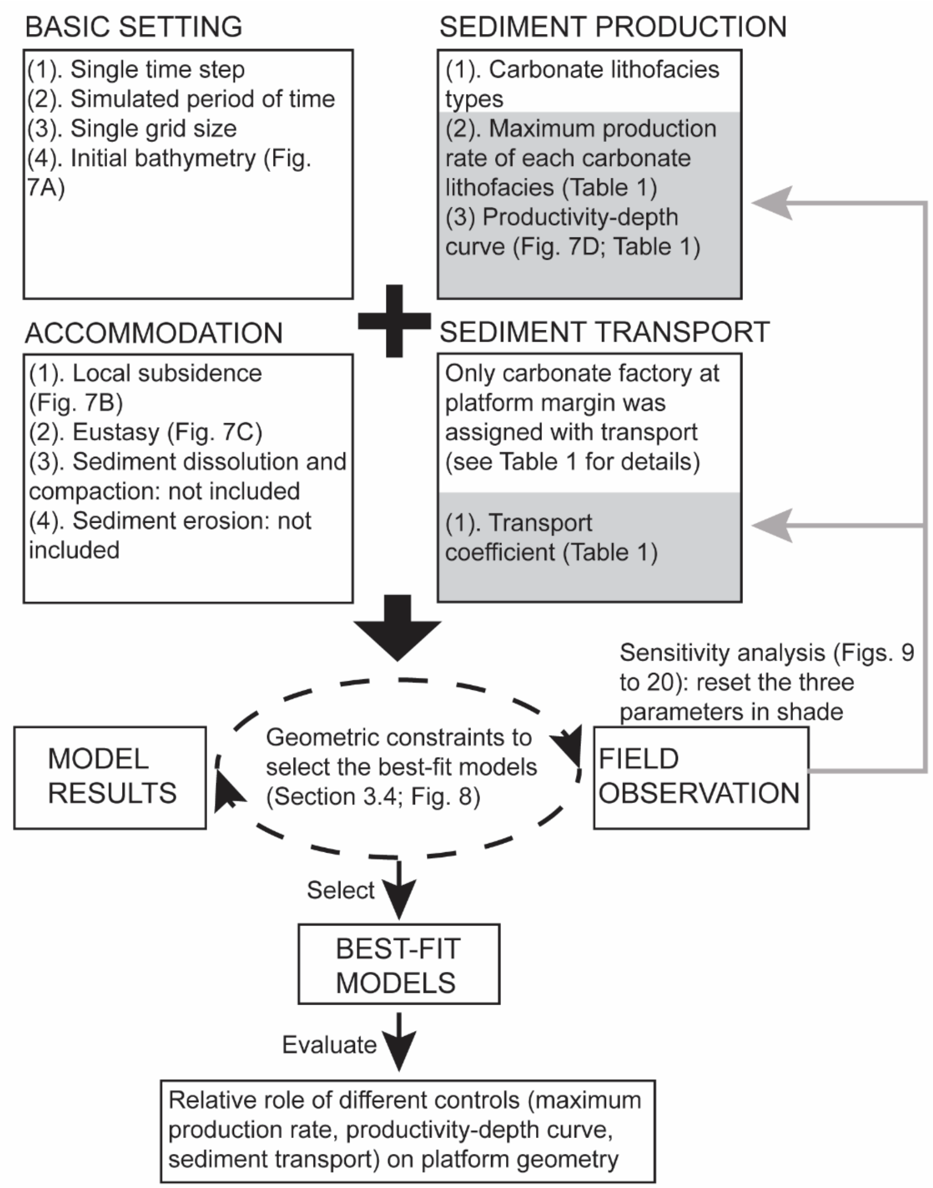

Figure 6. Workflow used to build models and assess the relative contribution of sediment production and sediment transport on the platform morphology of the GBG. Sensitivity analysis was performed through changing the maximum production rate, productivity-depth curve, and transport coefficient of a carbonate lithofacies (gray arrows and shade). Simulations are compared to field data through geometric constraints.

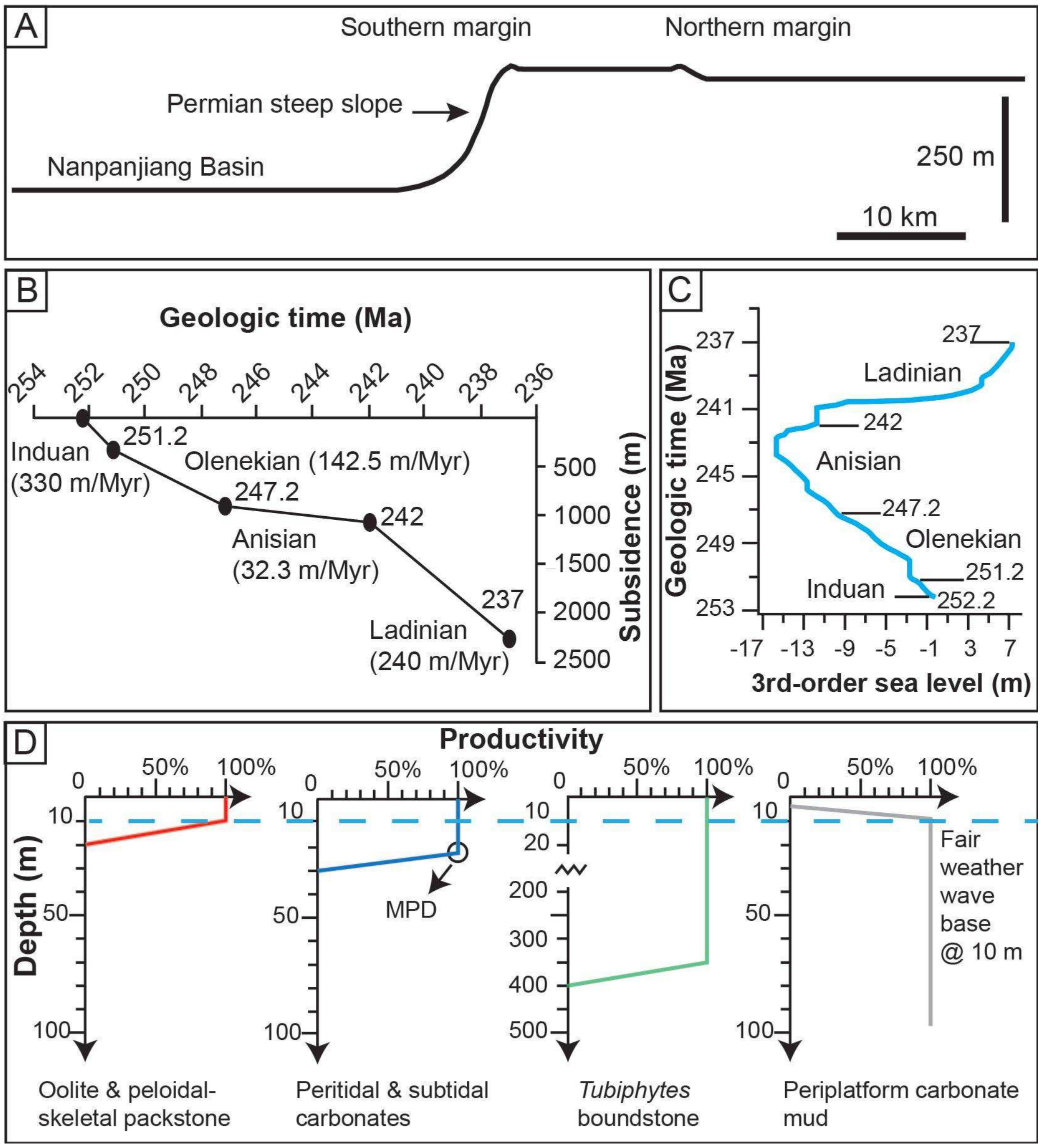

Figure 7. Model input parameters. (A) Initial bathymetry, antecedent topography inherited from the latest Permian (also see Figure 2B). (B) Local subsidence rate during the simulation period (Minzoni et al., 2013). (C) 3rd-order of eustasy fluctuations during the simulation period (Haq et al., 1987). (D) Productivity-depth curve of different carbonate factories. Fair-weather wave base is set to be at 10 m. Note a turning point on the productivity-depth curve of peri/subtidal carbonates represent its own maximum productivity depth (MPD). Periplatform carbonate mud is parameterized to reflect density cascading described by (Wilson and Roberts, 1995, 1992).

Local subsidence calculated from measured stratigraphic sections in the platform interior and at the margin (Minzoni et al., 2013; Fig. 5) was input as a constant value as shown in Figure 7B. Stratal thickness for each modeled stage was constrained using an established chemostratigraphic, biostratigraphic, chronostratigraphic, and lithostratigraphic framework (Kelley et al., 2020; Lehrmann et al., 2015b, 1998; Payne et al., 2004).

Model input used global 3rd-order sea level fluctuations following the curve of Haq et al. (1987; Fig. 7C) that is integrated into DIONISOS. High-frequency sea-level fluctuations affect facies distributions at the high-frequency cycle scale (e.g., Busson et al., 2019) but have little influence on platform morphology in large carbonate platforms (Bosence et al., 1994; Williams et al., 2011); thus, the use of the Haq et al. (1987) is sufficient for the purposes of this study. The rates of 3rd order eustatic fluctuations are one to two orders of magnitude lower (~2 m/Myr during the Induan; ~2.5 m/Myr during the Olenekian; ~1.5 m/Myr during the Anisian; ~3.2 m/Myr during the Ladinian) than the subsidence required for the sediment accumulation of each modeled stage (~330 m/Myr during the Induan; ~142.5 m/Myr during the Olenekian; ~32.3 m/Myr during the Anisian; ~240 m/Myr during the Ladinian; Minzoni et al., 2013). In this context the role of 3rd-order sea level variation on gross trends in accommodation is much less important than that of local subsidence.

Subaerial diagenetic features are present in the GBG (Lehrmann et al., 1998; Li et al., 2012). However, the lack of major biostratigraphic and chemostratigraphic gaps confirms that the GBG did not undergo subaerial erosion at a scale that would impact the broad objectives of this study (Lehrmann et al., 2015b, 1998; Meyer et al., 2011; Payne et al., 2004). For this reason, sediment loss related to subaerial exposure was not incorporated into subsidence corrections.

Aside from 25,000 yr, models of the Induan with longer (125,000 yr) and shorter (5,000 yr) temporal resolutions were also initially conducted and compared in order to find the one for satisfying the main purpose of this study with acceptable computational duration of running models. The main differences among the models relate to variations of slope thickness at a scale of tens of meters, implying that the modeled overall platform morphology is not sensitive to temporal resolutions in a significant manner. Therefore, 25,000 yr was selected due to its relevant duration of running a model (~1.7 hours) and properly mimicking the overall platform morphology.

3.2 Sediment production

DIONISOS simulates carbonate sediment production by specifying a maximum production rate (MPR in m/Myr) for a given lithofacies type, and then multiplying this rate at each grid cell (m^2) and time step (Myr) by coefficients (unitless) that depend on environmental parameters (water depth, wave energy) or geologic time (Granjeon and Joseph, 1999). Eventual sediment accumulation *in situ* is the result of sediment production deducting the amount of sediment transport (see Section 3.3). Based on Lehrmann et al.'s (1998) facies description and Payne et al.'s (2006) point counting results, we used five lithofacies types to model carbonate sediment production: (1) Oolite; (2) Peritidal-subtidal carbonates; (3) Periplatform carbonate mud; (4) *Tubiphytes* boundstone; and (5) Peloidal-skeletal packstone-grainstone (Fig. 7D; Table 1).

The lower bound of MPR of each carbonate lithofacies is approximated by the measured thickness of a carbonate lithofacies divided by the duration of time over which it was deposited (long-term accumulation rates; Schlager, 2003), neglecting correction for compaction and dissolution. A subset of carbonate lithofacies was included in the model for each stage based on the observed distribution of facies through the platform. For the Induan and Olenekian models, the lithofacies included are peritidal-subtidal carbonates, oolite, and periplatform carbonate mud (Fig. 3B; Table 1). For the Anisian simulations, the carbonate lithofacies modeled on the platform margin and upper slope was the *Tubiphytes* boundstone, while peritidal-subtidal carbonates were kept on the platform interior (Fig. 3B; Table 1). During the Ladinian, peloidal-skeletal packstone-grainstone was the carbonate lithofacies at the platform margin (Fig. 3B; Table 1). The depositional characteristics and the tested parameter range of each carbonate lithofacies are summarized in Table 1. For the simulations presented herein, the depth dependence of sediment production in each lithofacies type was modeled by specifying a depth above which productivity is still at its highest value (Fig. 7D; e.g., Bosence et al., 1994; Bosence and Waltham, 1990), herein termed maximum productivity depth (MPD). The productivity of a lithofacies, except for the periplatform carbonate mud, was assumed to remain at 100% from sea level to the MPD. Below this depth, productivity for the factories was assumed to decline linearly to zero over an interval of 5 to 50 m depending on the type of carbonate lithofacies (Fig. 7D). Currently, no studies have established a widely accepted productivity-depth curve for microbial *Tubiphytes* boundstone and criteria to precisely determine the productivity at a given depth is lacking. The influence of the productivity-depth curve of *Tubiphytes* boundstone on model output was explored via sensitivity analysis.

Because there is no field evidence showing abundant, *in situ* carbonate mud production on the slope during the Early Triassic, most of the fine-grained carbonate mud accumulated on slope and basin during the growth of the GBG is interpreted to have been sourced from the platform top and margin. Although periplatform mud may originate from the platform top, it is transported to the slope and basin through a vertical settling process in which mud is suspended across different water depths (c.f. density cascading in Wilson and Roberts, 1995, 1992). To reflect the vertical settling process and suspension of fine-grained sediments across different water depths, periplatform carbonate mud was parameterized differently, with a high rate of sediment production and accumulation in deeper water (up to hundreds of meters) depending on the coeval estimated maximum bathymetry in the deep basin (Bosence and Waltham, 1990; Fig. 7D). During sensitivity analyses, multiple MPD values were tested. No siliciclastic sediment supply was included in the model runs because siliciclastic turbidites did not reach the platform in the Bianyang syncline area until the Late Triassic (Lehrmann et al., 2015a). Lateral facies variation in the output was achieved through differences in percentage of simulated facies, water depth, hydrodynamic energy, and salinity (e.g., Kolodka et al., 2015).

3.3 Sediment transport

DIONISOS simulates transport and downslope re-deposition of platform-margin carbonates by a slope-driven transport equation that approximates advective transport of sediments as a function of the local slope angle, thickness of produced sediment (in meters; see Section 3.2 for sediment production), and a transport coefficient (m^2/kyr) in each grid cell after each time step (Myr) for each carbonate lithofacies (Granjeon and Joseph, 1999). The transport coefficient controls the capacity of each carbonate lithofacies to be transported for a given slope, integrating influences of sediment size, density, shape, and degree of syndepositional cementation to the substrate. Slope deposits of the GBG are primarily sourced from (1) the platform margin in the Induan, Olenekian, and Ladinian and (2) the platform margin and upper slope in the Anisian. Periplatform mud was assumed to be exported from the margins to the slope, and the volume shed from the interior to the slope was assumed to be negligible as the interior has a vast depositional area in comparison to the slope. In addition, the flat platform interior lacks any slope that would drive sediment transport basinward in DIONISOS. Therefore, peritidal carbonates in the platform interior were assumed to remain on the platform top without significant erosive transport to the basin (Table 1). A wide range of transport coefficient values was examined in model runs to assess the potential impact of sediment transport on platform geometry during different stages of platform accumulation (Table 1).

3.4 Geometric constraints used to select best-fit models

Sediment production of the shallow-water platform interior carbonate lithofacies for a given stage was set to be equal to or slightly greater (i.e., several hundred m/Myr more) than the coeval subsidence rate in order to avoid drowning within the model (Table 1). Sensitivity analysis was conducted by varying the MPR, MPD, and transport coefficient for the margin and slope factories. Simulation outcomes were compared to observed field data through geometric properties of the simulated carbonate platforms (see details below).

Because (1) the Permian to Middle Triassic lower slope and basin facies to the south of the GBG at Bangeng is not exposed (Li et al., 2012; Lehrmann et al., 2020; Fig. 3) and (2) limited data is available about the stratigraphic thicknesses of different lithofacies prior to catastrophic margin collapse at the southern margin, model-data comparison was conducted using observations from the platform interior, northern margin, and northern slope. The geometric properties used to compare model output to field observation are: (1) difference in thickness between the models and field measurements at each of three stratigraphic sections (Figs. 3B and 5; true thickness difference for Dajiang section in the platform interior, Rungbao section nearby the platform margin, and isochore difference for Guandao section at the slope) for each simulated time interval; (2) progradation distance of the platform margin relative to the Rungbao section (platform margin is defined as the point marked by abrupt decline from the platform top to the slope); (3) migration distance of the toe of slope relative to Guandao section (the toe of slope is defined as the point at which the slope angle drops below 1.4° (Heezen et al., 1959); and (4) maximum slope angle. Because simulated 3D morphologies of the GBG at different stages do not vary along the platform margin within the 2 km-wide model and because the geological exposure along the Bianyang syncline is effectively two-dimensional, 2D transects through the model output were used for model-data comparison and are displayed for simplicity.

Table 1. Characteristics and tested value range of different carbonate lithofacies used to reconstruct the morphology of the GBG and conduct sensitivity analysis.

Carbonate factory type	**Gross depositional environment**	**Tested range of maximum production rate (m/Myr)**	**Best-fit maximum production rate (m/Myr)**	**Tested range of maximum productivity depth (m)**	**Best-fit maximum productivity depth (m)**	**Tested range of transport coefficient (km^2/kyr)**	**Best-fit transport coefficient (km^2/kyr)**
Oolite	High energy, shallow water, platform margin	200 to 5000 (Induan, Fig. 9), 100 to 4400 (Olenekian, Fig. 12) (Harris, 1979)	500 (Induan), 200 (Olenekian)	1 to 15 (Fig. 10, Induan), 1 to 15 (Fig. 13, Olenekian; Harris et al., 2018; Harris, 1979)	10 (Induan and Olenekian)	0.001 to 0.32 (Induan, Fig. 11), 0.001 to 0.25 (Olenekian, Fig. 14)	0.004 (Induan), 0.001 (Olenekian)
Peri/subtidal carbonates	Low to moderate energy, platform interior, shallow water		Fixed: 600 (Induan), 200 (Olenekian), 300 (Anisian and Ladinian)		15 (fixed in all ages of the Early Triassic)	0	0
Periplatform carbonate mud	Low energy, slope and basin margin, moderate to deep water		20 (from Induan to Ladinian)		400	0	0
Tubiphytes boundstone	Independent on light, low to high energy, shallow to deep water, platform margin and upper slope	100 to 1800 (Anisian, Fig. 15; Enos, 1991)	300	10 to 1000 (Fig. 16; Marangon et al., 2011; Preto et al., 2017)	350	0.0004 to 0.032 (Fig. 17)	0.0004
Peloidal-skeletal packstone	High energy, shallow water, platform margin	100 to 5000 (Ladinian; Fig. 18)	650	1 to 14 (Fig. 19)	10	0.0001 to 0.0032 (Fig. 20)	0.0001

4. RESULTS

4.1 Maximum production rate of Induan oolite

The modeled Induan platform morphology is very sensitive to the MPR of the oolite at the platform margin (Fig. 9). Increasing the MPR increases the amount of sediment accumulated on the slope and therefore increases the isochore thickness of the slope in model runs (Guandao section in Fig. 9A), which results in basinward movement of the toe of slope (Fig. 9B) and decrease of the maximum clinoform angle from 21.6° to 8.9° (Fig. 9C). Meanwhile, the sediment accumulation in the distal basin increases by tens of meters.

All criteria used for model-data comparison display insensitivity of the platform morphology to two value ranges of MPR of oolite (600 to 1500 m/Myr and 2000 m/Myr onward; Fig. 9A to C) aside from increased sediment accumulation in the more distal basin at a scale of several meters. Values greater than 2000 m/Myr are at or beyond the greatest value reported from modern Bahamian oolite (2740 m/Myr from Harris, 1979), while the corresponding simulated margin and toe of slope positions are strikingly fixed (Fig. 8A and Fig., 9B, H, and I).

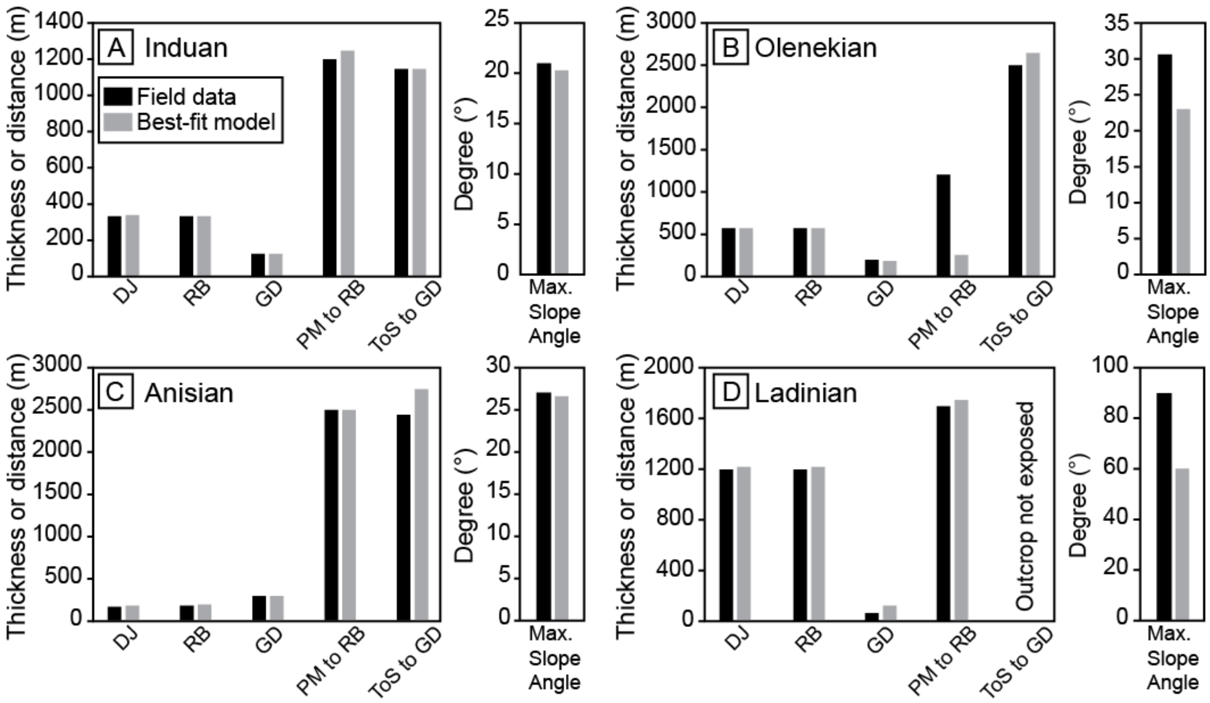

Figure 8. Comparison between field data and best-fit models of different stages. (A) The Induan. (B) The Olenekian. (C). The Anisian. (D). The Ladinian. Abbreviation: DJ = Dajiang section thickness; RB = Rungbao section thickness; GD = Guandao section thickness; PM to RB = Distance from platform margin to Rungbao section; ToS to GD = Distance from toe of slope to Guandao section.

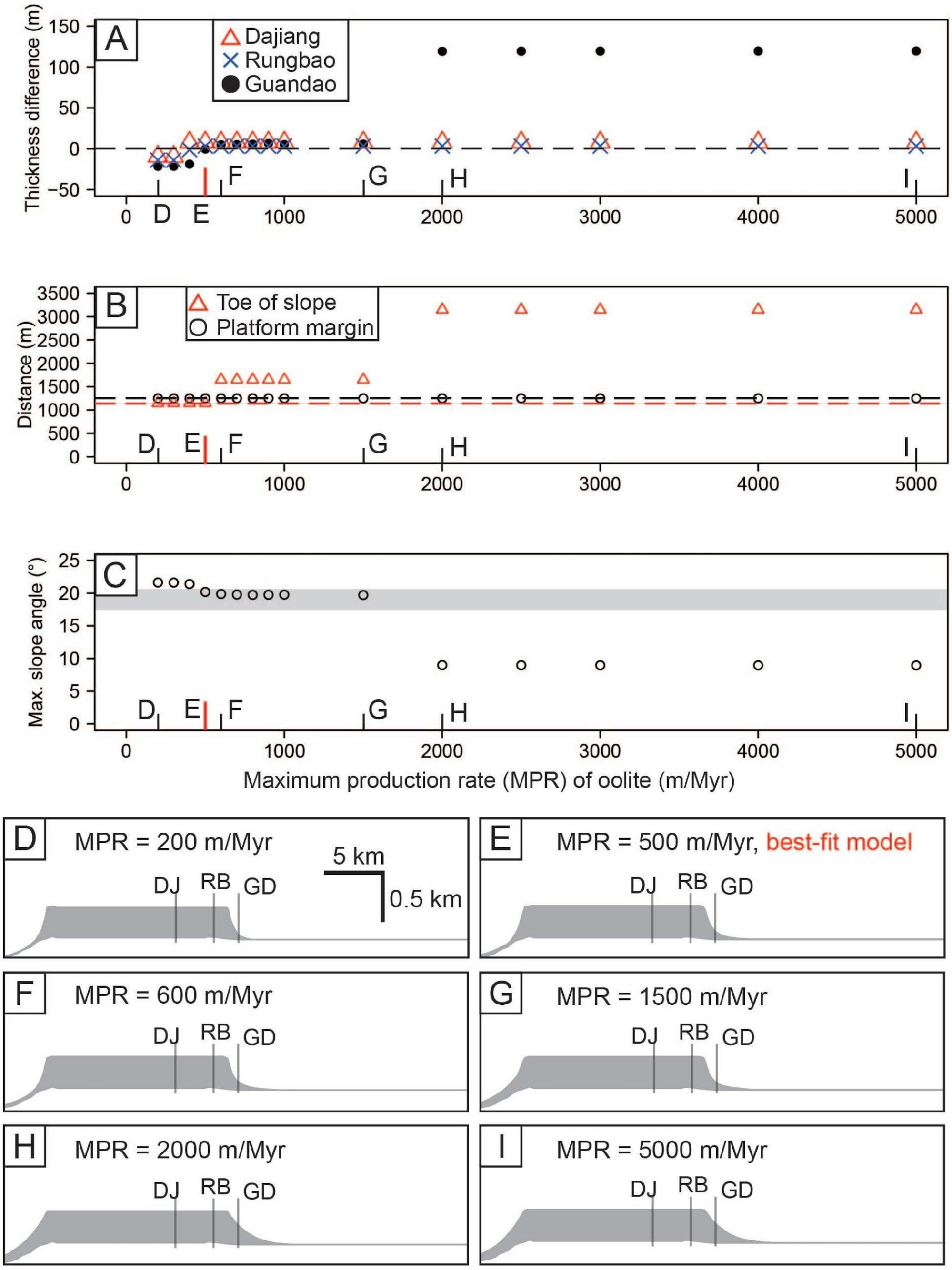

Figure 9. Control of maximum production rate (MPR) of the Induan oolite on platform geometry. (A) Thickness difference of Dajiang, Rungbao, and Guandao sections between field measurement and models with increased MPR. Capital D to I in (A) through (C) corresponds to different MPR of oolite that are included from Figure 9D to I. (B) Platform margin progradation distance relative to Rungbao section (~1200 m from field observation, horizontal black dashed line) and toe of slope migration distance relative to Guandao section (~1150 m from field observation, horizontal red dashed line) as a response to the increased MPR. (C) Maximum clinoform slope angle with increased MPR of oolite. Note a gray horizontal bar (17° to 21°) is the range of maximum clinoform slope angle from field measurement. (D) to (I) Simulated platform morphology when the MPR is at 200, 500, 600, 1500, 2000, and 5000 m/Myr. Stratigraphic section locations shown: DJ = Dajiang, RB = Rungbao, GD = Guandao. Gray area shows modeled sediment accumulation during model run and resulting platform morphology.

4.2 Maximum productivity depth of Induan oolite

The Induan platform morphology is less sensitive to the MPD of oolite within the value range examined (Fig. 10). Shallower values of the MPD yield simulated slopes that accumulate less sediment than observed in the field; deeper values generate simulated slopes with sediment accumulation slightly higher than observed (Fig. 10A). The position of platform margin and toe of slope does not vary across this range of parameter values (Fig. 10B), and the maximum clinoform slope angle is relatively invariant, decreasing from 21.6° to 20° with increasing MPD, very close to the measured maximum clinoform slope angle of 17° to 21° (Fig. 10C).

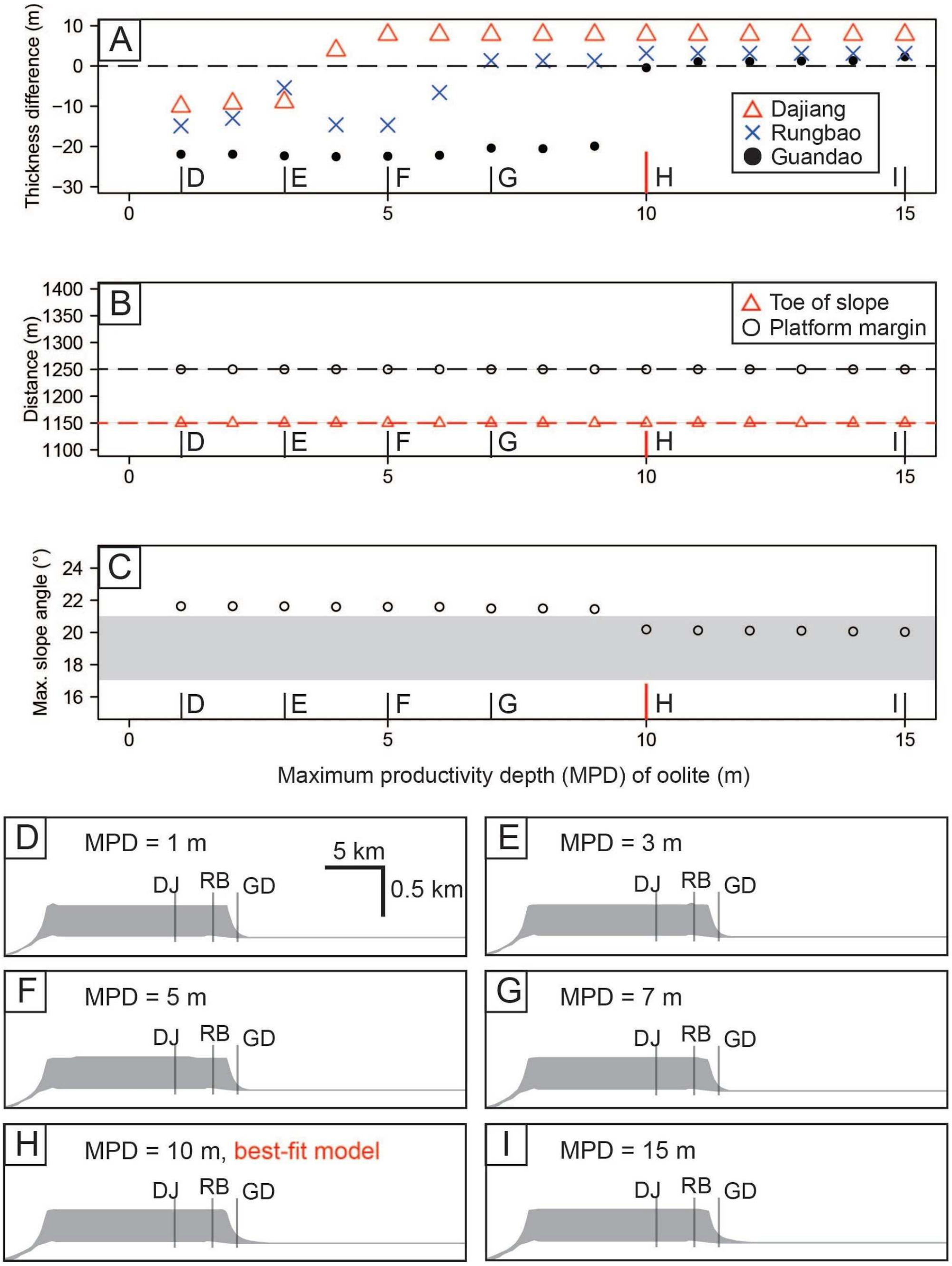

Figure 10. Control of maximum productivity depth (MPD) of the Induan oolite on platform geometry. (A) Thickness difference of Dajiang, Rungbao, and Guandao sections between field measurement and models with increased MPD. Capital D to I in (A) through (C) corresponds to different MPD of oolite that are included from Figure 10D to I. (B) Platform margin progradation distance relative to Rungbao section (~1200 m from field observation, horizontal black dashed line) and toe of slope migration distance relative to Guandao section (~1150 m from field observation, horizontal red dashed line) as a response to increased MPD. (C) Maximum clinoform slope angle with increased MPD of oolite. Note a gray horizontal bar (17° to 21°) is the range of maximum clinoform slope angle from field measurement. (D) to (I) Simulated platform morphology when the MPD is at 1, 3, 5, 7, 10, and 15 m. Stratigraphic section locations shown: DJ = Dajiang, RB = Rungbao, GD = Guandao. Gray area shows modeled sediment accumulation during model run and resulting platform morphology.

4.3 Transport coefficient of Induan oolite

Sediment transport has a pronounced impact on the overall platform geometry (Fig. 11). The platform morphology shifts from a high-relief, steep-sloped platform to a more ramp-like bank when the transport coefficient increases from the lowest simulated value (0.001 km^2/kyr) to the highest simulated value (0.32 km^2/kyr) (Fig. 11C to I). With low but increasing transport coefficients, from 0.001 to 0.02 km^2/kyr, the platform margin retreats while the toe of slope moves towards the basin (Fig. 11B and D to G). In contrast, for transport coefficients greater than 0.02 km^2/kyr, the simulated toe of slope and platform margin both step back because the retreat of the platform margin rapidly decreases the area of highest sediment production and thus the overall sediment production of the platform (Fig. 11B, H and I). Meanwhile, the sediment accumulation in the distal basin increases at a scale of tens of meters.

The difference in thickness between simulated and observed slope sediment accumulation at the Guandao section increases from -75.7 m to 24.1 m when the transport coefficient increases by an order of magnitude, from 0.001 to 0.01 km^2/kyr (Fig. 11A, D to F). When the modeled transport coefficient is increased by another order of magnitude, from 0.01 to 0.32 km^2/kyr, the difference between modeled and observed slope sediment accumulation at the Guandao location decreases from 24.1 to -5.6 m to reflect the lower overall productivity on the platform due to retreat of the margin (Fig. 11A). The Induan platform morphology is more sensitive to changing the transport coefficients of ooids than to MPR or MPD over the range of values examined.

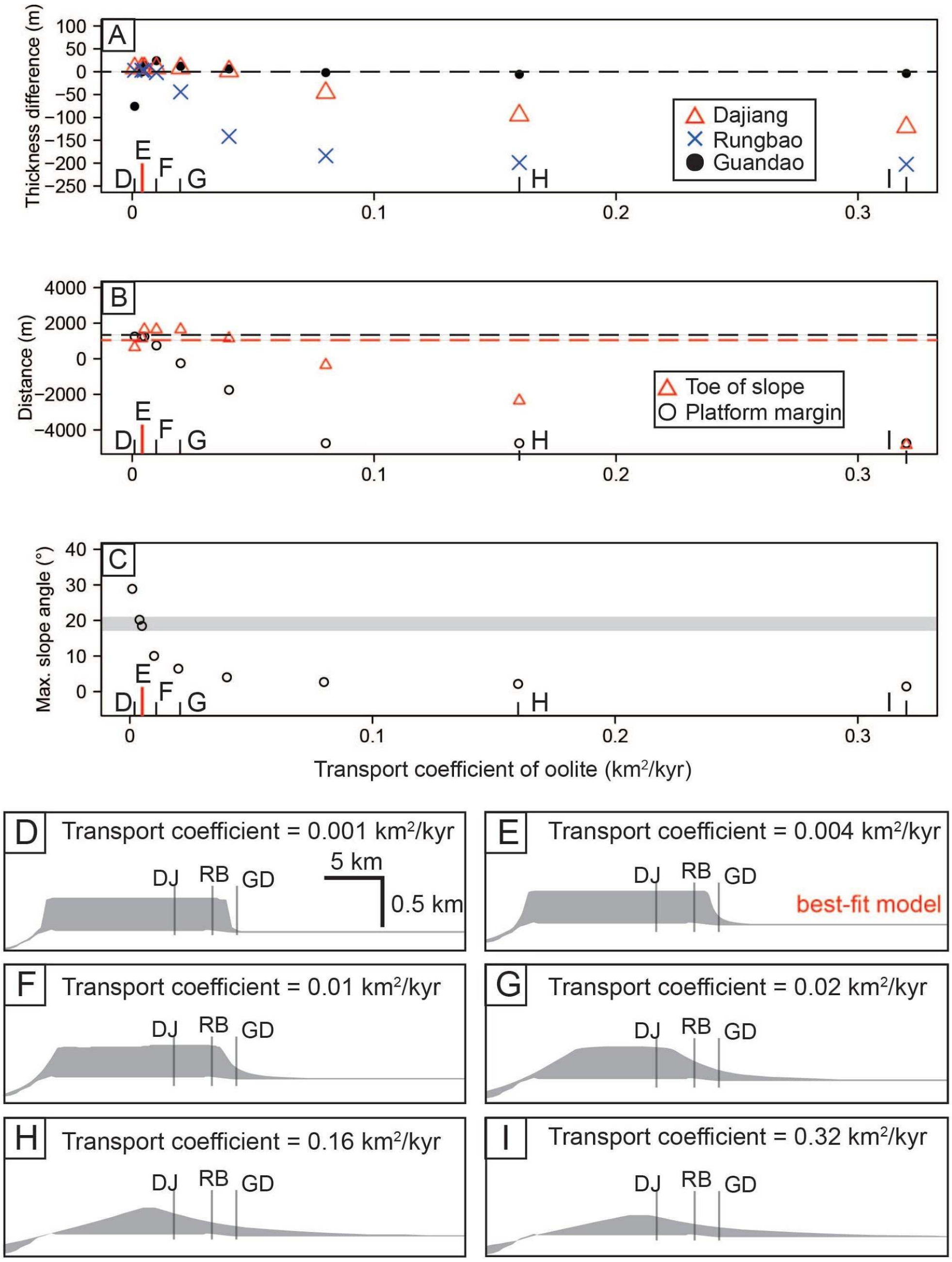

Figure 11. Control of transport coefficient of the Induan oolite on platform geometry. (A) Thickness difference of Dajiang, Rungbao, and Guandao sections between field measurement and models with increased transport coefficient. Capital D to I in (A) through (C) corresponds to different transport coefficient of oolite that are included from Figure 11D to I. (B) Platform margin progradation distance relative to Rungbao section (~1200 m from field observation, horizontal black dashed line) and toe of slope migration distance relative to Guandao section (~1150 m from field observation, horizontal red dashed line) as a response to increased transport coefficient. (C) Maximum clinoform slope angle with increased transport coefficient of oolite. Note a gray horizontal bar (17° to 21°) is the range of maximum clinoform slope angle from field measurement. (D) to (I) Simulated platform morphology when the transport coefficient is at 0.001, 0.004, 0.01, 0.02, 0.16, and 0.32 km^2/kyr. Stratigraphic section locations shown: DJ = Dajiang, RB = Rungbao, GD = Guandao. Gray area shows modeled sediment accumulation during model run and resulting platform morphology.

4.4 Maximum production rate of Olenekian oolite

The carbonate factory type at the platform margin does not change between the Induan and Olenekian. The response of Olenekian platform morphology to the MPR of the oolite at the platform margin is similar to that of the Induan. The Olenekian platform morphology is sensitive to the MPR of the oolite at the platform margin (Fig. 12). Increasing the MPR increases the amount of sediment accumulated on the slope and therefore increases the isochore thickness of the slope in model runs (Guandao section in Fig. 12A), which results in basinward movement of the toe of slope and platform margin (Fig. 12B) and decrease of the maximum clinoform angle from 26° to 17° (Fig. 12C). Meanwhile, sediment accumulation in the distal basin increases at a scale of tens of meters.

Notably, all criteria used for comparing simulation results to observed field data display insensitivity of the platform morphology to maximum production rate for values ranging from 800 to 4400 m/Myr (Fig. 12A to C), while the corresponding simulated margin and toe of slope positions together are nearly fixed (Fig. 12B). Coeval distal basinal sediment accumulation increases slightly. The mismatch of platform margin position between field data and best-fit models (Fig. 8B) is most likely caused by limitations of the model grid size, which prevents the model from effectively simulating the transport of ooids from the shoals or the movement of shoals over distances smaller than the grid scale.

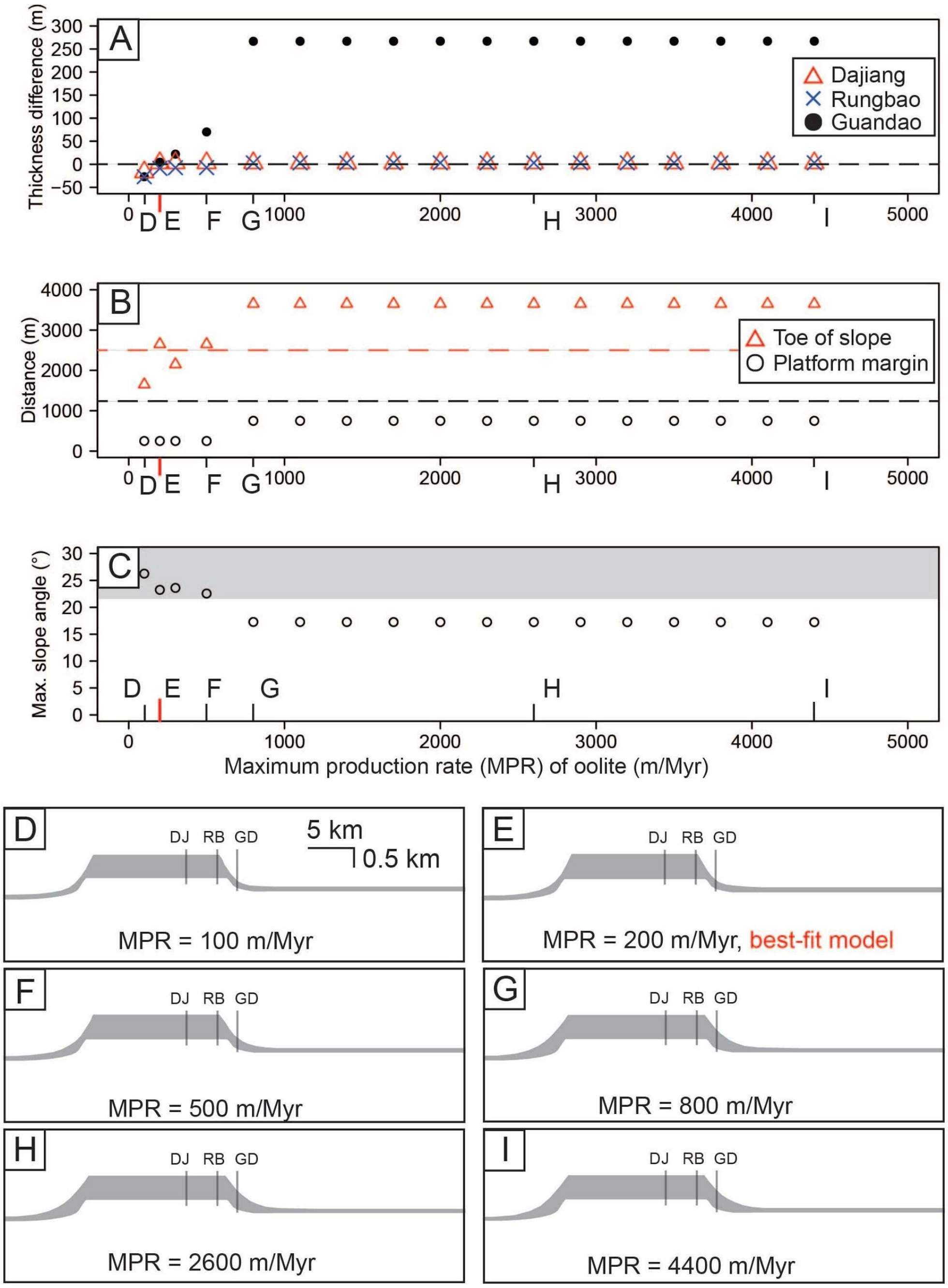

Figure 12. Control of maximum production rate (MPR) of the Olenekian oolite on platform geometry. (A) Thickness difference of Dajiang, Rungbao, and Guandao sections between field measurement and models with increased MPR. Capital D to I in (A) through (C) corresponds to different MPR of oolite that are included from Figure 12D to I. (B) Platform margin progradation distance relative to Rungbao section (~1200 m from field observation, horizontal black dashed line) and toe of slope migration distance relative to Guandao section (~2500 m from field observation, horizontal red dashed line) as a response to the increased MPR. (C) Maximum clinoform slope angle with increased MPR of oolite. Note a gray horizontal bar (23° to 31°) is the range of maximum clinoform slope angle from field measurement. (D) to (I) Simulated platform morphology when the MPR is at 100, 200, 500, 800, 2600, and 4400 m/Myr. Stratigraphic section locations shown: DJ = Dajiang, RB = Rungbao, GD = Guandao. Gray area shows modeled sediment accumulation during model run and resulting platform morphology.

4.5 Maximum productivity depth of Olenekian oolite

The Olenekian platform morphology is less sensitive to the MPD of oolite within the value range examined (Fig. 13). Shallower values of the MPD yield simulated slopes that accumulate less sediment than observed in the field; deeper values generate simulated slopes with sediment accumulation slightly greater than observed (Fig. 13A). The positions of the platform margin and toe of slope do not vary across this range of parameter values (Fig. 13B), and the maximum clinoform slope angle is relatively invariant, decreasing from 26° to 23° with increasing MPD (Fig. 13C).

507

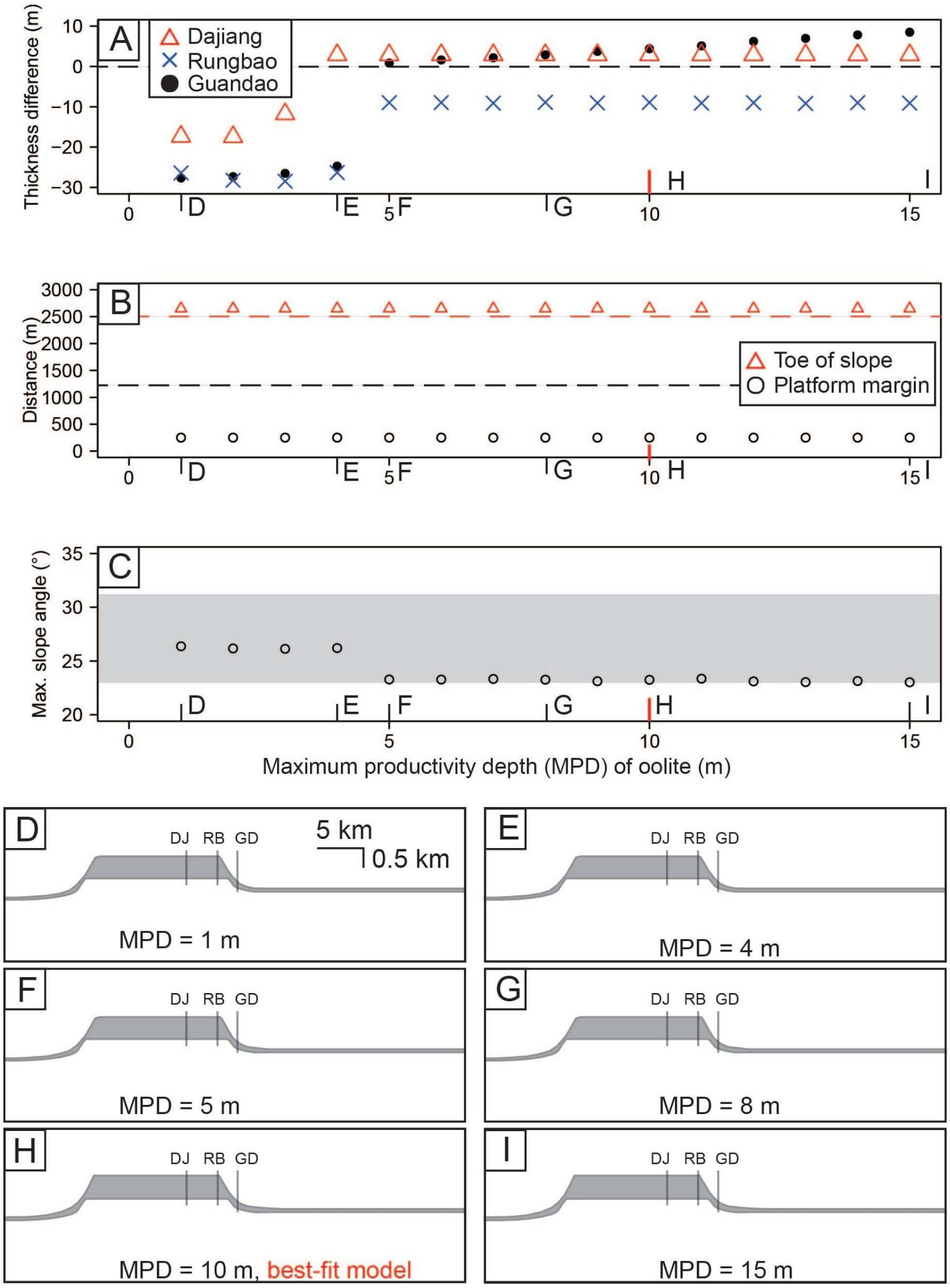

508 **Figure 13**. Control of maximum productivity depth (MPD) of the Olenekian oolite on platform geometry. (A) Thickness difference of Dajiang, Rungbao, and Guandao sections between field measurement and models with increased MPD. Capital D to I in (A) through (C) corresponds to different MPD of oolite that are included from Figure 13D to I. (B) Platform margin progradation distance relative to Rungbao section (~1200 m from field observation, horizontal black dashed line) and toe of slope migration distance relative to Guandao section (~2500 m from field observation, horizontal red dashed line) as a response to increased MPD. (C) Maximum clinoform slope angle with increased MPD of oolite. Note a gray horizontal bar (23° to 31°) is the range of maximum clinoform slope angle from field measurement. (D) to (I) Simulated platform morphology when the MPD is at 1, 4, 5, 8, 10, and 15 m. Stratigraphic section locations shown: DJ = Dajiang, RB = Rungbao, GD = Guandao. Gray area shows modeled sediment accumulation during model run and resulting platform morphology.

4.6 Transport coefficient of Olenekian oolite

The Olenekian platform morphology is more sensitive to changing the transport coefficients of ooids than to MPR or MPD over the range of values examined (Fig. 14). The platform morphology shifts from a high-relief carbonate platform to a more ramp-like bank when the transport coefficient increases from the lowest simulated value (0.001 km^2/kyr) to the highest simulated value (0.25km^2/kyr) (Fig. 14C to I). Meanwhile, the sediment accumulation in the distal basin increases at a scale of tens of meters. With low but increasing transport coefficients, from 0.001 to 0.016 km^2/kyr, the platform margin retreats while the toe of slope moves towards the basin (Fig. 14B and D to G). In contrast, for transport coefficients greater than 0.016 km^2/kyr, both the toe of slope and platform margin step back (Fig. 14B, H and I). Meanwhile, as the platform margin retreats (Fig. 14B), the thickness difference of all three sections decreases as more sediments are transported to the distal basin (Fig. 14A). The maximum slope angle increases slightly when the transport coefficient exceeds 0.032 km^2/kyr (Fig. 14C). This increase occurs because the simulated maximum slope angle in the Olenekian is inherited from the antecedent Induan shelf break as sediments bypass the steep shelf break and move towards the basin.

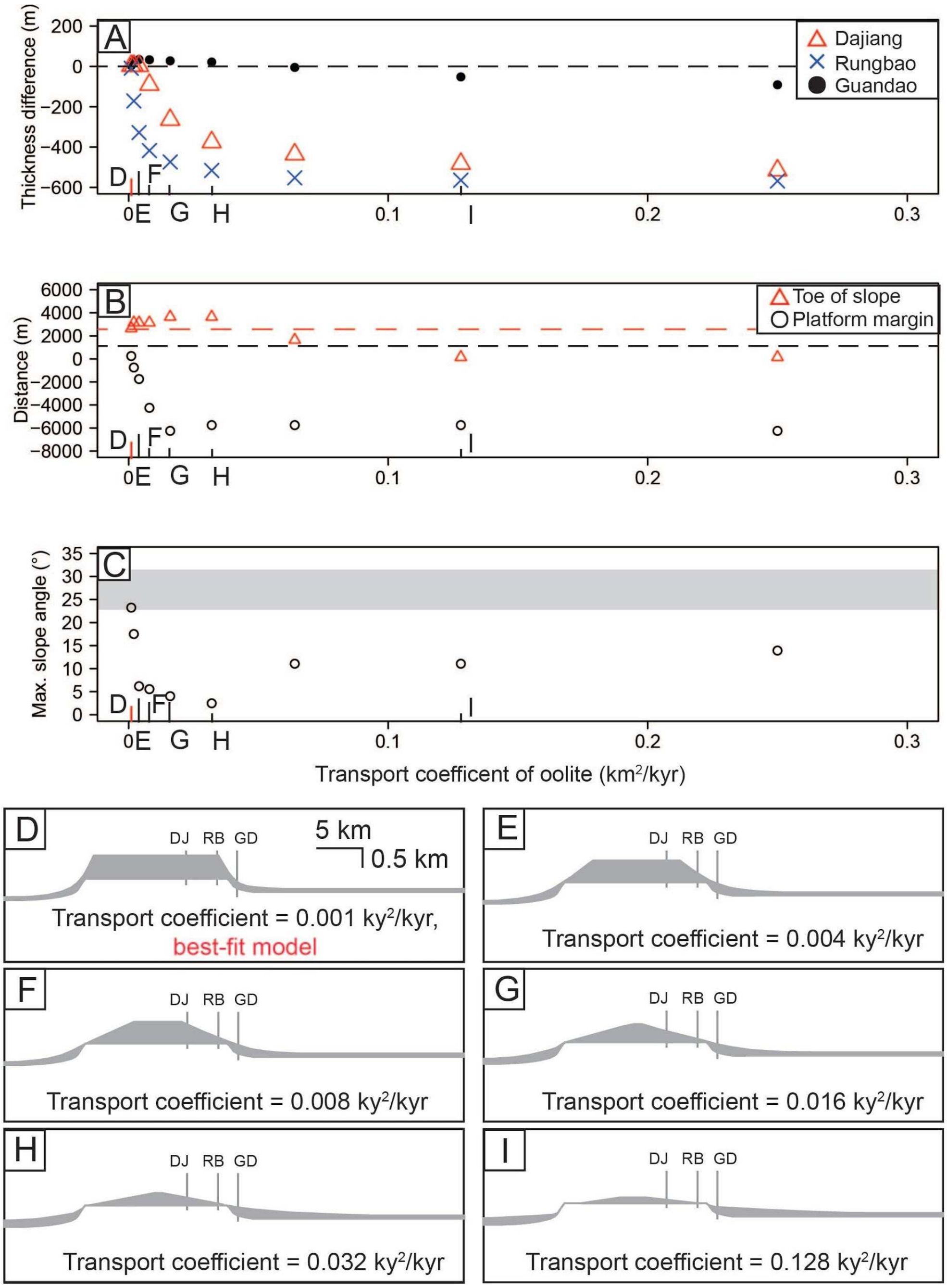

Figure 14. Control of transport coefficient of the Olenekian oolite on platform geometry. (A) Thickness difference of Dajiang, Rungbao, and Guandao sections between field measurement and models with increased transport coefficient. Capital D to I in (A) through (C) corresponds to different transport coefficient of oolite that are included from Figure 14D to I. (B) Platform margin progradation distance relative to Rungbao section (~1200 m from field observation, horizontal black dashed line) and toe of slope migration distance relative to Guandao section (~2500 m from field observation, horizontal red dashed line) as a response to increased transport coefficient. (C) Maximum clinoform slope angle with increased transport coefficient of oolite. Note a gray horizontal bar (23° to 31°) is the range of maximum clinoform slope angle from field measurement. (D) to (I) Simulated platform morphology when the transport coefficient is at 0.001, 0.004, 0.008, 0.016, 0.032, and 0.128 km^2/kyr. Stratigraphic section locations shown: DJ = Dajiang, RB = Rungbao, GD = Guandao. Gray area shows modeled sediment accumulation during model run and resulting platform morphology.

4.7 Maximum production rate of Anisian *Tubiphytes* boundstone

The Anisian platform morphology is very sensitive to the MPR of the *Tubiphytes* boundstone (Fig. 15). Increasing the MPR of *Tubiphytes* boundstone at the platform margin and upper slope from 100 to 1800 m/Myr increases the difference between simulated and observed slope thickness from -99.6 to 644.1 m (Fig. 15A) and increases the simulated maximum clinoform angle from 18.2° to 35° (Fig. 15C). The toe of slope and platform margin both move approximately linearly basinward with increasing MPR (Fig. 15B). Notably, the available vertical accommodation at the Guandao location is entirely filled when the maximum production rate exceeds 900 m/Myr; in other words, at production rates above 900 m/Myr the platform margin progrades beyond the position of the Guandao section (Fig. 15G to I). Meanwhile, the sediment accumulation in the distal basin increases at a scale of tens of meters.

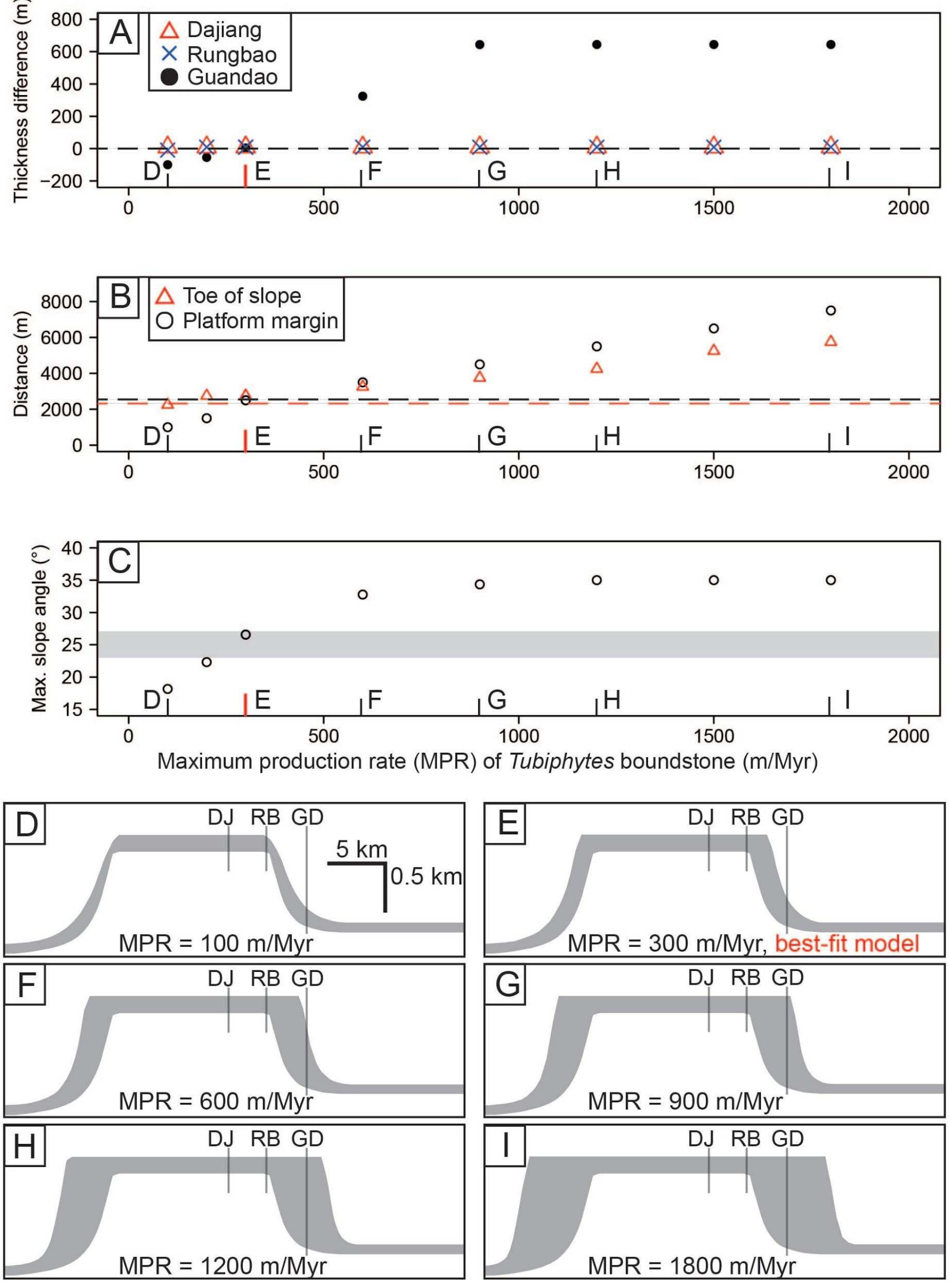

Figure 15. Control of maximum production rate (MPR) of the Anisian *Tubiphytes* boundstone on platform geometry. (A) Thickness difference of Dajiang, Rungbao, and Guandao sections between field measurement and models with increased MPR. Capital D to I in (A) through (C) corresponds to different MPR of *Tubiphytes* boundstone that are included from Figure 15D to I. (B) Platform margin progradation distance relative to Rungbao section (~2500 m from field observation, horizontal black dashed line) and toe of slope migration distance relative to Guandao section (~2450 m from field observation, horizontal red dashed line) as a response to increased MPR. (C) Maximum clinoform slope angle with increased MPR of *Tubiphytes* boundstone. Note a gray horizontal bar (23° to 27°) is the range of maximum clinoform slope angle from field measurement. (D) to (I) Simulated platform morphology when the MPR is at 100, 300, 600, 900, 1200, and 1800 m/Myr. Stratigraphic section locations shown: DJ = Dajiang, RB = Rungbao, GD = Guandao. Gray area shows modeled sediment accumulation during model run and resulting platform morphology.

4.8 Maximum productivity depth of Anisian *Tubiphytes* boundstone

The Anisian platform morphology is also very sensitive to the MPD of the *Tubiphytes* boundstone, which appears to have been active to several hundreds of meters of water depth (Fig. 16; Keim and Schlager, 2001; Kelley et al., 2020; Marangon et al., 2011; Preto et al., 2017). Therefore, the MPD of the *Tubiphytes* boundstone was varied from 50 to 1000 m in the simulations (Fig. 16). Both the platform margin and toe of slope migrate basinward under all values of the MPD (Fig. 16B). The difference in slope thickness between simulations and the measured section at the Guandao location at the slope shows a positive correlation with the MPD, ranging from -155 to 655.1 m (Fig. 16A). The maximum slope angle is less sensitive to the variations of the MPD, changing from 17.7° to 26.8° across the simulations (Fig. 16C). The northern margin area in the basin is entirely filled when the MPD is greater than 1000 m (Fig. 16I).

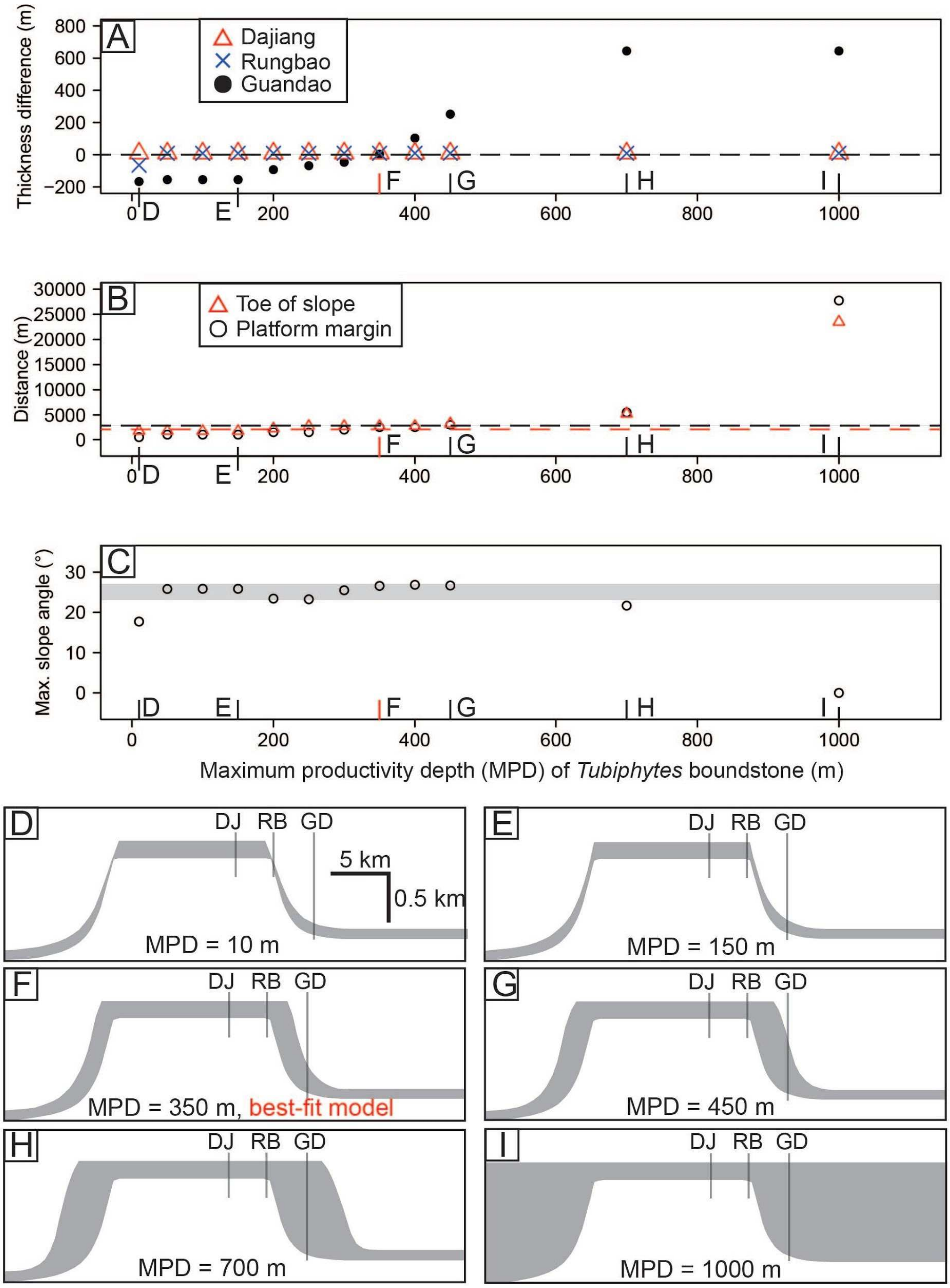

Figure 16. Control of maximum productivity depth (MPD) of the Anisian *Tubiphytes* boundstone on platform geometry. (A) Thickness difference of Dajiang, Rungbao, and Guandao sections between field measurement and models with increased MPD. Capital D to I in (A) through (C) corresponds to different MPD of *Tubiphytes* boundstone that are included from Figure 16D to I. (B) Platform margin progradation distance relative to Rungbao section (~2500 m from field observation, horizontal black dashed line) and toe of slope migration distance relative to Guandao section (~2450 m from field observation, horizontal red dashed line) as a response to increased MPD. (C) Maximum clinoform slope angle with increased MPD of *Tubiphytes* boundstone. Note a gray horizontal bar (23° to 27°) is the range of maximum clinoform slope angle from field measurement. (D) to (I) Simulated platform morphology when the MPD is at 10, 150, 350, 450, 700, and 1000 m. Stratigraphic section locations shown: DJ = Dajiang, RB = Rungbao, GD = Guandao. Gray area shows modeled sediment accumulation during model run and resulting platform morphology.

4.9 Transport coefficient of Anisian *Tubiphytes* boundstone

The Anisian platform morphology is also sensitive to the transport coefficient assigned to the *Tubiphytes* boundstone (Fig. 17). As the transport coefficient of *Tubiphytes* boundstone increases from 0.0004 to 0.002 km^2/kyr, the modeled slope thickness increases, exceeding the measured isochore value at Guandao by 3.3 to 420.1 m (Fig. 17A). The location of the platform margin does not change appreciably across this range of transport coefficients, but the toe of slope migrates farther basinward at higher transport coefficients (Fig. 17B) while the maximum clinoform slope angle decreases from 26.6° to 12.9° (Fig. 17C). When the transport coefficient of *Tubiphytes* boundstone further increases from 0.002 to 0.032 km^2/kyr, the platform margin steps back conspicuously while the toe of slope moves several kilometers basinward (Fig. 17B) and the maximum slope angle decreases from 12.9° to 3.7° (Fig. 17C). Consistent with field evidence for mostly *in situ* sediment production, the best fit is obtained with the lowest transport coefficient (Fig. 17D).

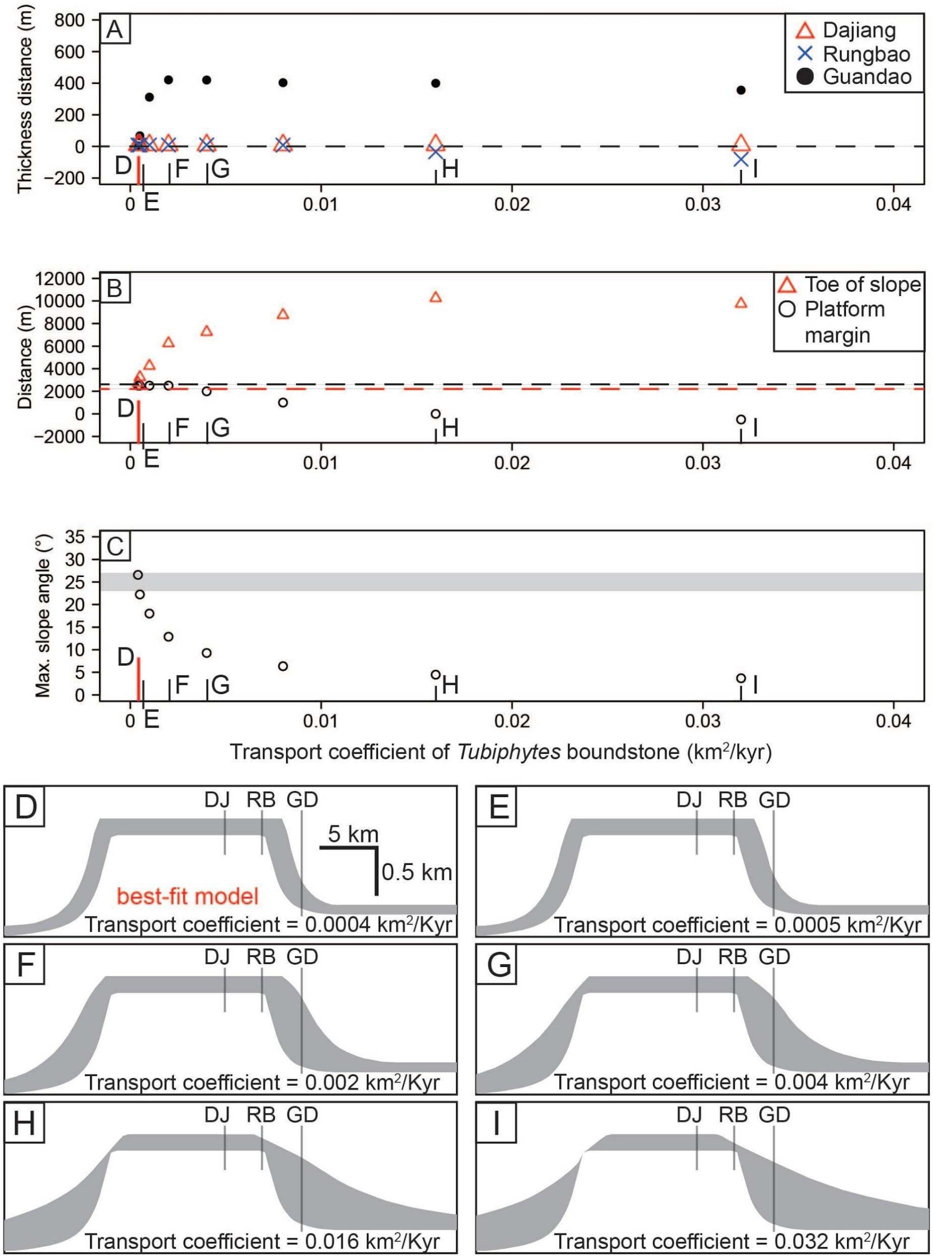

Figure 17. Control of sediment transport coefficient of the Anisian *Tubiphytes* boundstone on platform geometry. (A) Thickness difference of Dajiang, Rungbao, and Guandao sections between field measurement and models with increased transport coefficient. Capital D to I in (A) through (C) corresponds to different sediment transport coefficient of *Tubiphytes* boundstone that are included from Figure 17D to I. (B) Platform margin progradation distance relative to Rungbao section (~2500 m from field observation, horizontal black dashed line) and toe of slope migration distance relative to Guandao section (~2450 m from field observation, horizontal red dashed line) as a response to increased transport coefficient. (C) Maximum clinoform slope angle with increased transport coefficient of *Tubiphytes* boundstone. Note a gray horizontal bar (23° to 27°) is the range of maximum clinoform slope angle from field measurement. (D) to (I) Simulated platform morphology when the transport coefficient is at 0.0004, 0.0005, 0.002, 0.004, 0.016, and 0.032 km^2/kyr. Stratigraphic section locations shown: DJ = Dajiang, RB = Rungbao, GD = Guandao. Gray area shows modeled sediment accumulation during model run and resulting platform morphology.

4.10 Maximum production rate of Ladinian peloidal-skeletal packstone

DIONISOS does not simulate an escarpment margin. The best-fit model in Sections 4.10 to 4.12 show a high-relief carbonate platform with an accretionary margin. However, it reasonably resembles the features of the Ladinian escarpment from the aspects of thickness of platform-top and slope sediment accumulation as well as distance of platform margin to Rungbao section (Fig. 8D) while lacking a surface of non-deposition upon which slope strata onlap.

The Ladinian platform morphology is sensitive to the MPR of the peloidal-skeletal packstone at the platform margin and the platform morphology transits from a pinnacle nucleating over the pre-existing Anisian platform interior (Fig. 18C and D) as the MPR increases from 100 to 350 m/Myr (Fig. 18E-H). The simulated platform morphology becomes essentially fixed when it exceeds 350 m/Myr (Fig. 18A and B) and the overall morphology does not vary except for an increase of tens of meters in thickness of basinal accumulation in more distal areas.

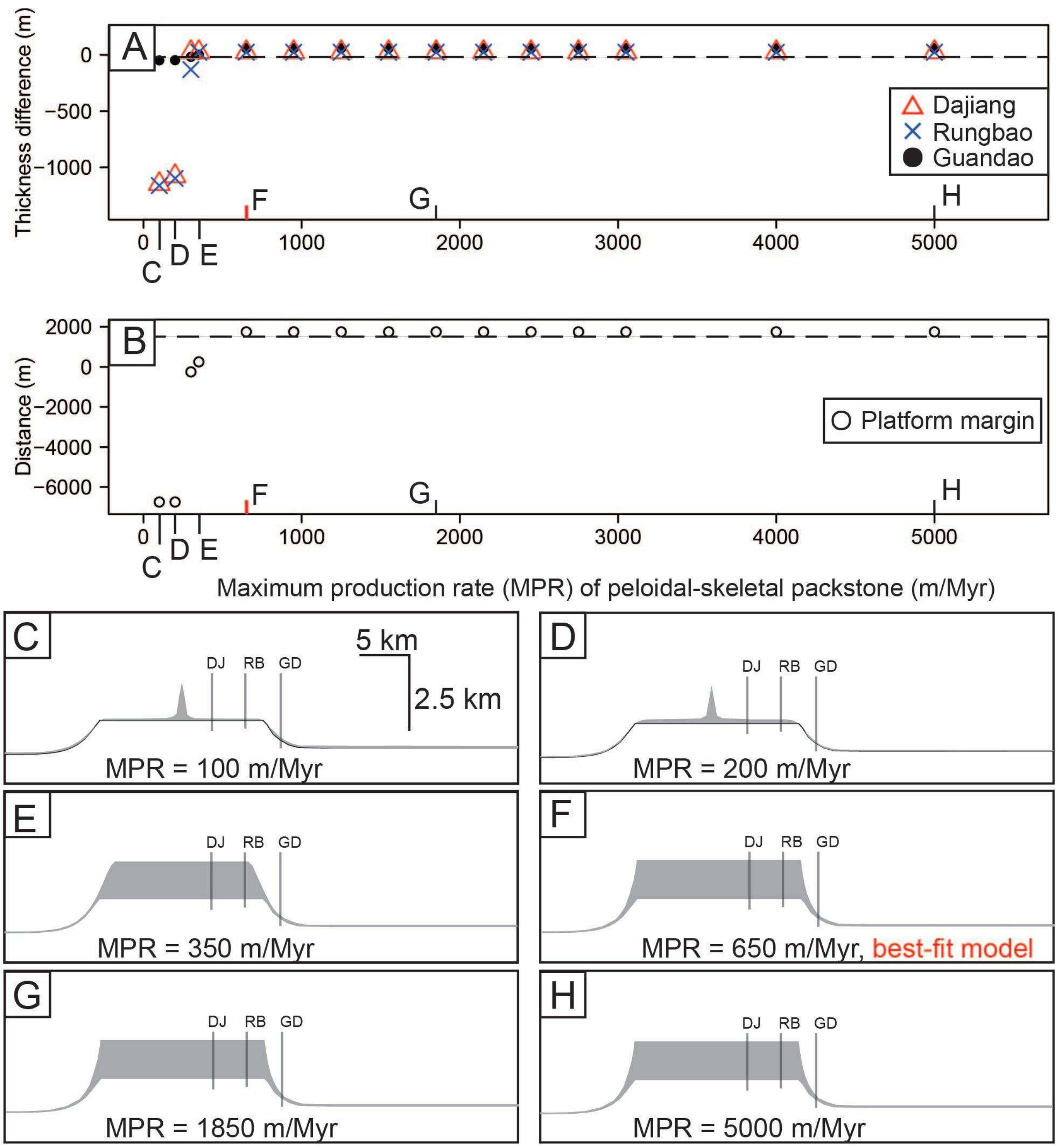

Figure 18. Control of maximum production rate (MPR) of the Ladinian peloidal-skeletal packstone on platform geometry. (A) Thickness difference of Dajiang, Rungbao, and Guandao sections between field measurement and models with increased MPR. Capital C to H in (A) and (B) corresponds to different MPR of peloidal-skeletal packstone that are included from Figure 18C to H. (B) Platform margin progradation distance relative to Rungbao section (~1700 m from field observation, horizontal black dashed line) as a response to the increased MPR. (C) to (H) Simulated platform morphology when the MPR is at 100, 200, 350, 650, 1850, and 5000 m/Myr. Stratigraphic section locations shown: DJ = Dajiang, RB = Rungbao, GD = Guandao. Gray area shows modeled sediment accumulation during model run and resulting platform morphology.

4.11 Maximum productivity depth of Ladinian peloidal-skeletal packstone

The Ladinian platform morphology is less sensitive to the MPD of oolite within the value range examined (Fig. 19). All the models with different tested MPD shows slightly thicker slope accumulation (Fig. 19A). Shallower values of the MPD (less than 5 m) still can form a high-relief platform, but its platform margin retreats approximately 250 m more than observed in field data. The position of platform margin does not migrate when the MPD is greater than 5 m (Fig. 19B) and other geometric constraints are also fixed (Fig. 19A). Basinal sediment thickness increases slightly when the MPD is greater than 5 m.

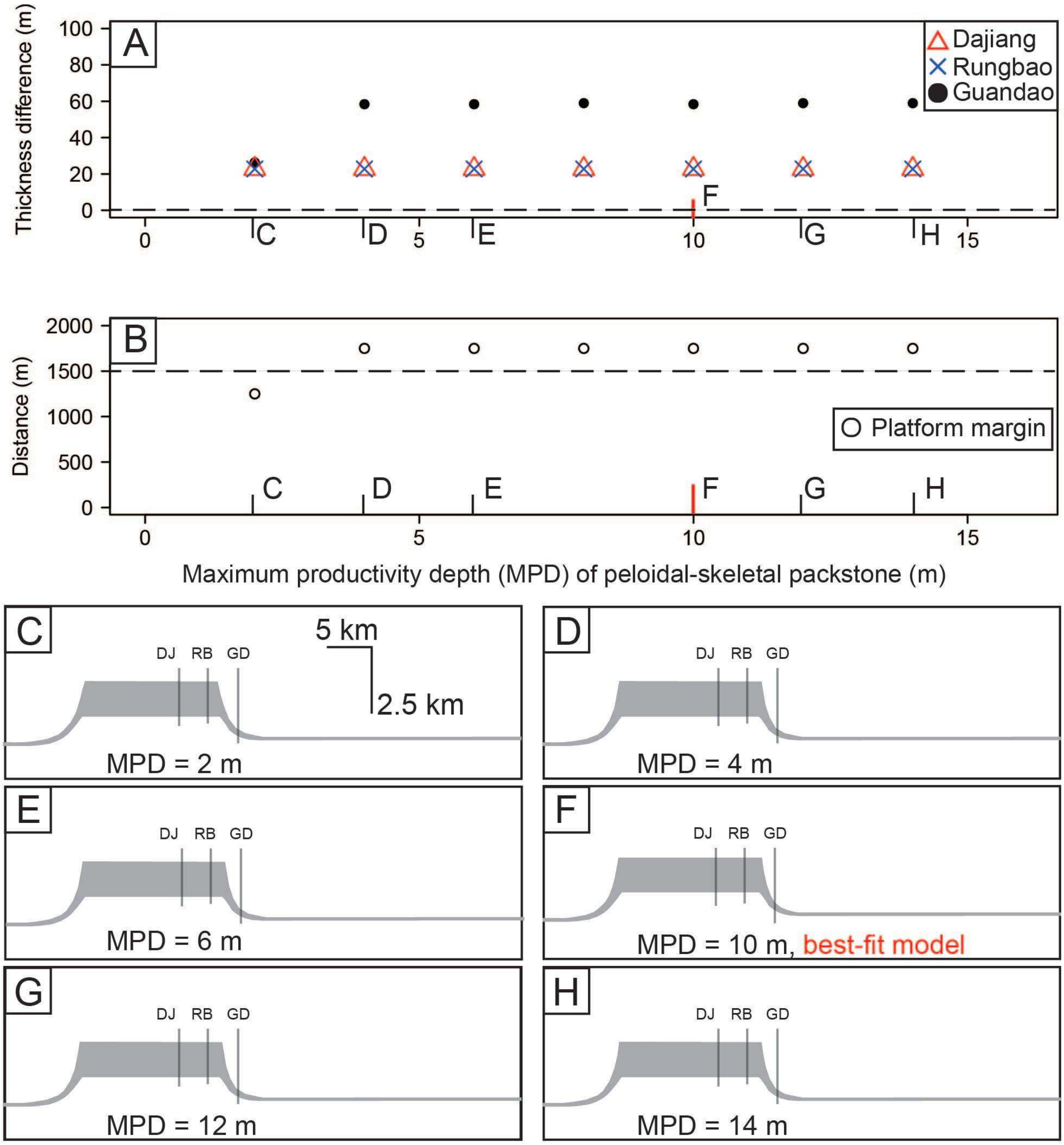

Figure 19. Control of maximum productivity depth (MPD) of the Ladinian peloidal-skeletal packstone on platform geometry. (A) Thickness difference of Dajiang, Rungbao, and Guandao sections between field measurement and models with increased MPD. Capital C to H in (A) and (B) corresponds to different MPD of peloidal-skeletal packstone that are included from Figure 19C to H. (B) Platform margin progradation distance relative to Rungbao section (~1700 m from field observation, horizontal black dashed line) as a response to the increased MPD. (C) to (H) Simulated platform morphology when the MPD is at 2, 4, 6, 10, 12, and 14 m. Stratigraphic section locations shown: DJ = Dajiang, RB = Rungbao, GD = Guandao. Gray area shows modeled sediment accumulation during model run and resulting platform morphology.

4.12 Transport coefficient of Ladinian peloidal-skeletal packstone

Sediment transport has a pronounced impact on the overall platform geometry (Fig. 20). The platform morphology shifts from a high-relief carbonate platform (Fig. 20A) to a drowned platform (Fig. 20H) when the transport coefficient increases from the lowest simulated value (0.0001 km^2/kyr) to the highest simulated value (0.0032 km^2/kyr) (Fig. 20C to H). With increasing transport coefficients, the platform margin retreats (Fig. 20B to H). The difference in thickness between simulated and observed slope sediment accumulation at the Guandao section decreases from 23 to -1000 m when the transport coefficient increases from 0.0001 to 0.0032 km^2/kyr (Fig. 20A, D to F).

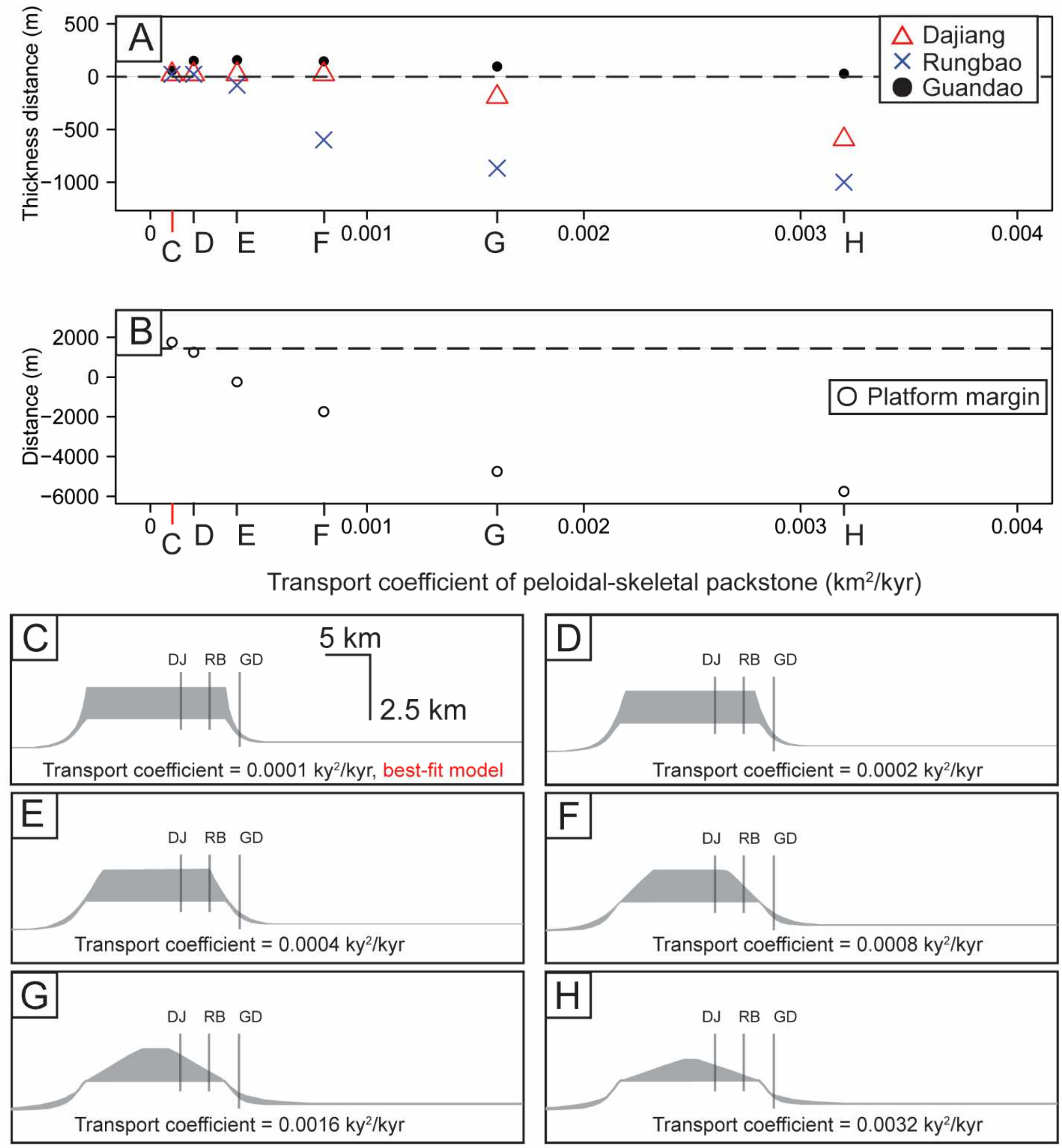

Figure 20. Control of sediment transport coefficient of the Ladinian peloidal-skeletal packstone on platform geometry. (A) Thickness difference of Dajiang, Rungbao, and Guandao sections between field measurement and models with increased transport coefficient. Capital C to H in (A) and (B) corresponds to different transport coefficient of peloidal-skeletal packstone that are included from Figure 20C to H. (B) Platform margin progradation distance relative to Rungbao section (~1700 m from field observation, horizontal black dashed line) as a response to the increased transport coefficient. (C) to (H) Simulated platform morphology when the transport coefficient is at 0.0001, 0.0002, 0.0004, 0.0008, 0.0016, and 0.0032 km^2/kyr. Stratigraphic section locations shown: DJ = Dajiang, RB = Rungbao, GD = Guandao. Gray area shows modeled sediment accumulation during model run and resulting platform morphology.

5. DISCUSSION

5.1 Controls on Early Triassic ramp to high-relief, steep-sloped platform transition of the GBG

The Lower Triassic morphology of the GBG is unusual in exhibiting a transition from a low-relief ramp to a high-relief, steep-sloped platform (Kelley et al., 2020) as ooids continued to develop in high-energy hydrodynamic environments during the transition while lacking any evidence of a metazoan or microbial reef margin or modification of the margin by synsedimentary tectonics. Similar ramp-to-shelf transitions in the rock record are typically associated with the development of a skeletal or microbial reef framework on the platform margin and/or slope [e.g., Cambrian Shady Dolomite carbonate platform in the US (Barnaby and Read, 1990); Permian Guadalupe Mountains in west Texas and New Mexico (Kerans et al., 2013; Tinker, 1998); Jurassic Djebel Bou Dahar platform in Morocco (Della Porta et al., 2013; Merino-Tomé et al., 2012; Verwer et al., 2009); Miocene platform in the Balearic Islands of Spain (Pomar, 2001)], and reef development is often interpreted as playing a causal role in this transition (Barnaby and Read, 1990; Pomar, 2001; Merino-Tomé et al., 2012; Kerans et al., 2013). In contrast, the Early Triassic margin of the GBG is an accretionary, steepening margin primarily composed of oolite stabilized and lithified by early marine cements (Figs. 4 and 5; Kelley et al., 2020).

To form a high-relief Early Triassic carbonate platform within the model, enough sediment must have been produced and stabilized on the platform top to compensate for the high rate of tectonic subsidence, while at the same time only a small amount of sediment produced on the platform top was transported to and accumulated on the slope. In the absence of a metazoan or microbial reef in the Early Triassic, enhanced early marine cementation causing partial lithification of grainy sediments can explain the limited transport of carbonate grains from the platform top to the slope. The high prevalence of precipitated primary fabrics in Lower Triassic carbonate accumulations, such as carbonate microbialites, ooids, and seafloor crystal fans (Fig. 4; Lehrmann, 1999; Li et al., 2019; Woods et al., 1999), points toward unusually high levels of carbonate saturation that would also have promoted syndepositional lithification and stabilization of the margin and/or lower slope (Van Der Kooij et al., 2010).

5.2 Implication of the Induan, Olenekian and Anisian geometry

The types of carbonate factories at the platform margin and upper slope in the Early Triassic (Induan and Olenekian) and Anisian are different. The Early Triassic platform margin is predominantly composed of ooids, whereas the Anisian margin and upper slope comprise *Tubiphytes* boundstone. If the transport coefficient is small (Fig. 11D to F), ooids can initially develop within a ramp geometry but continue to form and accumulate on the platform margin while a transition from a ramp to a high-relief, steep-sloped platform occurs. Under this scenario, the overall platform growth rate does not scale linearly with sediment production potential (i.e., MPR). Instead, the platform growth rate asymptotes (Fig. 21; also see Figs. 9D to G, 12D to G, and 18C to F), because accommodation is filled in the area where the platform-top factory would otherwise be active (Fig. 21; also see Figs. 9H and I, 12G to I, and 18F to H where platform morphology does not change with increased MPR). Interestingly, for carbonate platforms whose sediments are mainly produced on the platform top, growth can also be limited by extremely efficient transport of sediments from the platform margin to the slope and basin. When such transport outpaces sediment production on the platform margin, it causes an ongoing reduction in the area of the platform-top carbonate factory, reducing the further production of sediment and leading to further retreat (Figs. 11, 14, and 20). The Anisian *Tubiphytes* boundstone on the slope does not experience similar growth limitation at low transport coefficient values because the lithofacies produces sediment directly into the basin along the slope and therefore does not become limited by accommodation at the site of sediment production (Della Porta et al., 2004; Keim and Schlager, 2001; Playton and Kerans, 2018; Verwer et al., 2009), consistent with the slope shedding model (Kenter et al., 2005). Low subsidence rates during the Anisian (Fig. 7B) would further favor progradation in response to any shedding of sediment from the platform top during this time.

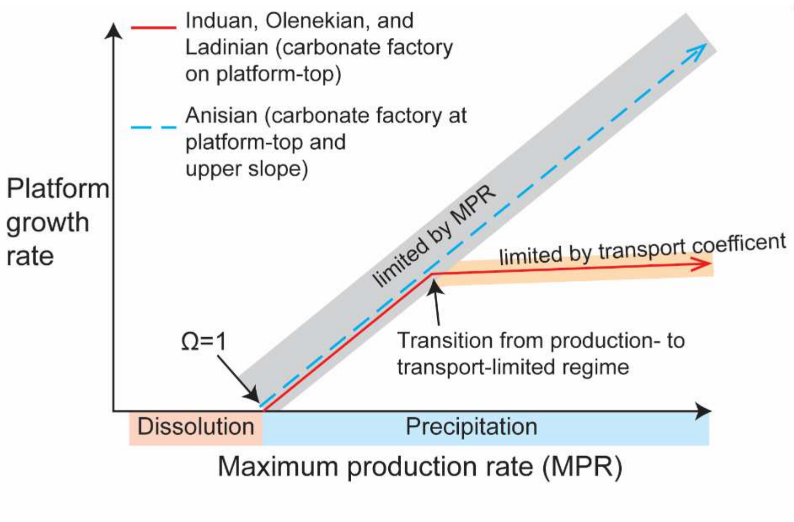

Figure 21. Platform growth rate responds differently to the maximum production rate depending on the location of the carbonate factory contributing sediment to the slope and the transport coefficient for the platform margin factory. The Induan, Olenekian, and Ladinian platform growth becomes limited by the transport coefficient when the maximum production rate becomes much larger than subsidence, such that accommodation on the platform top is completely filled and further sediment production requires the transport of sediment from the platform margin to the slope and basin. Anisian platform geometry is mainly controlled by the maximum production rate (production-limited regime; dashed blue line in the gray shade) because *Tubiphytes* boundstone grew into available accommodation directly on the slope and did not require any transport between the site of sediment production and the site of available accommodation.

Limited transport of ooids after production due to early lithification by marine cementation can explain why the GBG was able to evolve from a low-relief ramp to a high-relief platform in the Early Triassic even in the absence of a metazoan or microbial reef at the platform margin and upper slope. This situation contrasts with the distribution of ooids and slope steepening of ancient and modern carbonate platforms. Ooids typically occur in either low-gradient carbonate ramp systems where ooids are dominantly developed near fair-weather wave base in inner/middle ramp area and muddy sediments become dominant distally (Gischler and Lomando, 2005; Marchionda et al., 2018; Pierre et al., 2010) or on steep-sided carbonate shelf systems where ooids develop at the platform margin but are perched on a pre-existing antecedent topography that was not dominantly constructed by oolite accumulation [e.g. Carboniferous Sierra del Cuera (Bahamonde et al., 2004; Della Porta et al., 2004), Jurassic Djebel Bou Dahar (Della Porta et al., 2013; Scheibner and Reijmer, 1999; Verwer et al., 2009), and Quaternary Bahamas (Harris et al., 2018; Rankey and Reeder, 2011). However, these classic depositional models are only partly compatible with the GBG, where the ooid factory dominated the platform margin during the transition from a low-relief bank to a high-relief platform. Furthermore, there was no syndepositional tectonic modification of the northern margin while the GBG steepened in the Early Triassic (Kelley et al., 2020; Lehrmann et al., 1998).

The Lower Triassic example of the GBG offers an example of accretionary steepening margin, which is composed mainly of oolite, without the sediment-stabilizing influence of metazoan and microbial reef builders (Kelley et al., 2020). Sensitivity analysis of the simulated Induan and Olenekian morphology to transport coefficient demonstrates that although reefs may be important in causing transitions of carbonate systems from ramps to high-relief steep-sloped platforms, other mechanism, such as early marine cementation, can result in a similar transition and the impact of early marine cementation must have been, quantitatively, of a similar magnitude to that of a metazoan or microbial reef in reducing the transport coefficient. Using the same approach to model other platforms will enable quantitative comparison of the parameters that best fit the GBG with those that best fit platforms that developed from ramps to high-relief, steep-sloped platforms in the presence of a metazoan reef.

5.3 Inevitability of the Ladinian high-relief margin

The best-fit Ladinian model reasonably resembles the coeval escarpment observed in the field (Fig. 8D), even though DIONISOS cannot strictly simulate a surface of non-deposition upon which slope strata onlap (Fig. 18F). The Ladinian high-relief platform develops in the model largely independently of the chosen values for MPR and MPD. The high relief of the platform top above the basin floor during this stage of growth constrained the possibilities for further progradation of the margin. As the GBG accreted in the Induan and Olenekian, shallow-water sediment production and transport to the slope in the Anisian was sufficient to cause progradation because the length of the slope was more limited and lower slope angles reduced the transport of sediment (Fig. 3B). By the Ladinian, the slope height was 1000 m and sediment production from shallow water and redeposition on the steep slope were not sufficient to fill the much larger accommodation. Models for the Ladinian platform geometry with accretionary margin indicate that when a carbonate platform continues to aggrade to form a high-relief topography, if carbonate sediment production is still dominantly sourced from shallow water and downslope transport is not enough to fill the slope profile, the carbonate platform would be highly prone to continue its high-relief steep geometry. Model simulations for the Ladinian demonstrate that steep-sided, high-relief platforms lacking slope factories are unlikely to prograde substantially under any conditions due to the vast amount of sediment required to enable progradation (Figs. 18 and 19).

Although numerical modeling results can generate the transition from a high-relief, steep-sloped platform back to a ramp by increasing the carbonate sediment transport rate while the platform does not drown (Fig. 17H and I), outcrop and subsurface analogs provide very few examples showing such a transition, and only in circumstances where basin sediment fills in the slope and basin environments, decreases slope height, and offers substrate for the adjacent platforms to prograde (Eberli et al., 2004; Enos et al., 1997; Lehrmann et al., 2015a) or where a younger ramp inherits and develops above the platform interior of an underlying steep-sloped carbonate platform (Phelps et al., 2015). Schlager (2005) implies that cold-water factories mostly produce loose sediment that can be relatively easily redistributed, but they have low sediment production rates. In contrast, tropical factories can have high sediment production rates, but they have more potential to be influenced by early marine cementation that would limit sediment transport. Therefore, in the geological record, very high sediment production and transport rates in carbonate depositional environments might be absent or rarely co-occur to form the transition from a high-relief, steep-sloped platform to a ramp.

5.4 Production- versus transport-limitation in the growth of carbonate platforms

Overall, modeling of the growth history of the GBG suggests that it grew under production-limited and transport-limited regimes in different stages (Fig. 21). For the Induan, Olenekian, and Ladinian, sediments are mainly sourced from platform-top carbonate factories. Given the local subsidence (Fig. 7B), platform growth rate was initially limited by intrinsic production capacity (MPR) of the platform interior and platform margin factories. Increasing MPR can increase growth rate of platform (dashed blue line and red line in the gray shade of Fig. 21) and cause variations of platform morphology (e.g. Figs. 9D to G, 12D to F, and 18C to E). However, increasing MPR does not continuously lead to coupled constant variations of platform growth rate if the coeval transport coefficient does not increase (Figs. 9H and I, 12G to I, and 18F to H; red line in the orange shade of Fig. 21). This change in behavior occurs because accommodation on the platform top becomes filled and transport of sediment into available accommodation in the adjacent basin becomes the factor limiting further sediment production and platform growth. The most likely explanation for this transport limitation in the Early Triassic is that early cementation limited the transport of sediments from the platform interior and platform margin and that by Ladinian time enormous slope height impeded any further progradation. By contrast, the platform growth during Anisian time is only related to a production-limited regime (blue dashed line in the gray shade of Fig. 21), when sediments are accumulated and cemented on slope and grew into available accommodation in the adjacent basin and the rate of platform growth was determined by the production capacity of the slope factory (e.g., Fig. 15). The preserved stratigraphic thickness of the platform interior section was used for model-data comparison without considering the effects of compaction and dissolution. The simplification indicates that the accommodation on platform-top in reality might be more quickly filled. Therefore, a transition from production-limited to transport-limited regime would be achieved more promptly.

6. CONCLUSIONS

The GBG displays variations of platform morphology, including ramp, steep-sloped platform, and bypass escarpment from the latest Permian to the Ladinian of the Middle Triassic. Because many potential controls on platform morphology are well-constrained from previous studies (e.g., local subsidence, global sea-level fluctuation, and geologic setting), the sensitivity of platform morphology to carbonate sediment production (sediment production rate and productivity-depth curve) and sediment transport can be investigated in detail through forward modeling. The Early Triassic transition from a ramp to a high-relief, steep-sloped platform occurred without the emplacement of a skeletal or microbial reef framework and or modification by synsedimentary tectonics in the northern margin of the GBG. It has been interpreted to be caused by low sediment transport related to stabilization of the margin by early marine cementation through simulation. Modeling of other platforms using the same approach can provide an avenue for comparing the magnitudes of optimal values for the GBG versus platforms that developed from ramps to high-relief, steep-sloped platforms in the presence of a metazoan reef.

Caution is therefore needed during seismic facies interpretation on high-relief geometries. Sensitivity analysis on the GBG suggests that the platform morphology is most sensitive to sediment transport, moderately sensitive to maximum production rate and least sensitive to maximum productivity depth for the same type of carbonate factory at the platform margin and/or on the slope. Models for the Ladinian platform geometry indicate that when a carbonate platform continues to aggrade to form a high-relief topography, if carbonate sediment production is still dominantly sourced from shallow water and downslope transport is not enough to fill the slope profile, the carbonate platform would have to continually maintain its high-relief. For carbonate platforms whose sediments predominantly originate from carbonate factories on the platform top and platform-top sediment production can catch up or even exceed accommodation created by subsidence and sea level change (like the GBG), platform growth rate is initially limited by production-capacity and subsequently limited by transport-capacity with increased maximum production rate of sediment. In contrast, platform growth rate may be limited by the production-capacity when the majority of sediments is sourced from a carbonate factory that can extend its growth depth to deep slope facies.

7. ACKNOWLEDGEMENTS

We greatly thank N. Adams, L. Stepchinski, D. Liu, and Q. Ning for field assistance. B. Kelley is thanked for sharing his data of Rungbao section and insights on the growth history of the platform at the northern margin. The research was supported by funding from Shell International E&P (PT31819) and Saudi Aramco (6500011100) grants to J.L. Payne and D.J. Lehrmann, and American Chemical Society

Petroleum Research Fund grants (45329-G8 to J.L. Payne and 53075-UR8 to D.J. Lehrmann). X. Li acknowledges extra support from AAPG Foundation John E. Kilkenny Memorial Grant, IAS Postgraduate Research Grant, and Stanford University McGee and Levorsen Research Grant. D. Cantrell is thanked for his discussion and suggestion on an earlier version of this manuscript. We would like to thank Beicip Inc. for the donation of a DIONISOS license. We are grateful to two reviewers, N. Preto and G. Warrlich, for their insightful and detailed comments that help improve the manuscript and to Associate Editor, M. Brandano for editing the manuscript.

REFERENCES

Bahamonde, J.R., Kenter, J.A.M., Della Porta, G., Keim, L., Immenhauser, A., Reijmer, J.J.G., 2004. Lithofacies and depositional processes on a high, steep-margined Carboniferous (Bashkirian-Moscovian) carbonate platform slope, Sierra del Cuera, NW Spain. Sediment. Geol. 166, 145–156. https://doi.org/10.1016/j.sedgeo.2003.11.019

Barnaby, R.J., Read, J.F., 1990. Carbonate ramp to rimmed shelf evolution: Lower to Middle Cambrian continental margin, Virginia Appalachians. Geol. Soc. Am. Bull. 102, 391–404. https://doi.org/10.1130/0016-7606(1990)102<0391:CRTRSE>2.3.CO;2

Barrett, S.J., Webster, J.M., 2017. Reef Sedimentary Accretion Model (ReefSAM): Understanding coral reef evolution on Holocene time scales using 3D stratigraphic forward modelling. Mar. Geol. 391, 108–126. https://doi.org/10.1016/j.margeo.2017.07.007

Bassant, P., Harris, P.M., 2008. Analyzing sequence architecture and reservoir quality of isolated carbonate platforms with forward stratigraphic modeling, in: Lukasik, J., Simo, J.A.T. (Eds.), Controls on Carbonate Platform and Reef Development. SEPM Special Publication 89, pp. 343–359. https://doi.org/10.2110/pec.08.89.0343

Bergmann, K.D., Grotzinger, J.P., Fischer, W.W., 2013. Biological influences on seafloor carbonate precipitation. Palaios 28, 99–115. https://doi.org/10.2110/palo.2012.p12-088r

Berra, F., Lanfranchi, A., Ronchi, P., Smart, P., Whitaker, F., 2016. Forward modeling of carbonate platforms: sedimentological and diagenetic constraints from an application to a flat-topped greenhouse platform (Triassic , Southern Alps , Italy). Mar. Pet. Geol. 78, 1–45. https://doi.org/10.1016/j.marpetgeo.2016.10.011

Bosence, D., Pomar, L., Waltham, D., Lankester, T., 1994. Computer modeling a Miocene carbonate platform, Spain. Am. Assoc. Pet. Geol. Bull. 78, 247–266. https://doi.org/https://doi.org/10.1306/BDFF9078-1718-11D7-8645000102C1865D

Bosence, D., Waltham, D., 1990. Computer modeling the internal architecture of carbonate platforms. Geology 18, 26–30. https://doi.org/10.1130/0091-7613(1990)018<0026

Burgess, P.M., Wright, V.P., 2003. Numerical forward modeling of carbonate platform dynamics: An evaluation of complexity and completeness in carbonate strata. J. Sediment. Res. 73, 637–652. https://doi.org/10.1306/020503730637

Busson, J., Joseph, P., Mulder, T., Teles, V., Borgomano, J., Granjeon, D., Betzler, C., Poli, E., Wunsch, M., 2019. High-resolution stratigraphic forward modeling of a Quaternary carbonate margin: Controls and dynamic of the progradation. Sediment. Geol. 379, 77–96. https://doi.org/10.1016/j.sedgeo.2018.11.004

Castell, J.M.C., Betzler, C., Rössler, J., Hüssner, H., Peinl, M., 2007. Integrating outcrop data and forward computer modelling to unravel the development of a Messinian carbonate platform in SE Spain (Sorbas Basin). Sedimentology 54, 423–441. https://doi.org/10.1111/j.1365-3091.2006.00843.x

Della Porta, G., Kenter, J.A.M., Bahamonde, J.R., 2004. Depositional facies and stratal geometry of an Upper Carboniferous prograding and aggrading high-relief carbonate platform (Cantabrian

Mountains, N Spain). Sedimentology 51, 267–295. https://doi.org/10.1046/j.1365-3091.2003.00621.x

Della Porta, G., Merino-Tomé, O., Kenter, J.A.M., Verwer, K., 2013. Lower Jurassic microbial and skeletal carbonate factories and platform geometry (Djebel Bou Dahar, High Atlas, Morocco), in: Klaas, V., Playton, T.E., Harris, P.M. (Eds.), Deposits, Architecture, and Controls of Carbonate Margin, Slope and Basinal Settings. SEPM Special Publication 105, pp. 237–263. https://doi.org/10.2110/sepmsp.105.01

Eberli, G.P., Betzler, C., Anselmetti, F., 2004. Carbonate Platform to Basin Transitions on Seismic Data and in Outcrops: Great Bahama Bank and the Maiella Platform Margin, Italy. Seism. imaging carbonate Reserv. Syst. AAPG Mem. 81 207–250.

Enos, P., 1991. Sedimentary parameters for computer modeling, in: Franseen, E.K., Watney, W.L., Kendall, C.G.S.C., Ross, W. (Eds.), Sedimentary Modeling: Computer Simulations and Methods for Improved Parameter Definition. Kansas Geological Survey Bulletin 233, pp. 63–99.

Enos, P., Jiayong, W., Yangji, Y., 1997. Facies distribution and retreat of Middle Triassic platform margin, Guizhou province, south China. Sedimentology 44, 563–584. https://doi.org/10.1046/j.1365-3091.1997.d01-34.x

Gervais, V., Ducros, M., Granjeon, D., 2018. Probability maps of reservoir presence and sensitivity analysis in stratigraphic forward modeling. Am. Assoc. Pet. Geol. Bull. 102, 613–628. https://doi.org/10.1306/0913171611517242

Gischler, E., Lomando, A.J., 2005. Offshore sedimentary facies of a modern carbonate ramp, Kuwait, northwestern Arabian-Persian Gulf. Facies 50, 443–462. https://doi.org/10.1007/s10347-004-0027-4

Granjeon, D., Joseph, P., 1999. Concepts and applications of a 3-D multiple lithology, diffusive model in stratigraphic modeling, in: Harbaugh, J.W., Watney, W.L., Rankey, E.C., Slingerland, R., Goldstein, R.H., Franseen, E.K. (Eds.), Numerical Experiments in Stratigraphy: Recent Advances in Stratigraphic and Sedimentologic Computer Simulations. SEPM Special Publication 62, pp. 197–209. https://doi.org/10.2110/pec.99.62.0197

Halfar, J., Godinez-Orta, L., Mutti, M., Valdez-Holguín, J.E., Borges, J.M., 2004. Nutrient and temperature controls on modern carbonate production: An example from the Gulf of California, Mexico. Geology 32, 213–216. https://doi.org/10.1130/G20298.1

Haq, B.U., Hardenbol, J., Vail, P.R., 1987. Chronology of fluctuating sea levels since the Triassic. Science (80-.). 235, 1156–1167. https://doi.org/10.1126/science.235.4793.1156

Harris, P. (Mitch), Diaz, M.R., Eberli, G.P., 2018. The Formation and Distribution of Modern Ooids on Great Bahama Bank. Ann. Rev. Mar. Sci. 11, 491–516. https://doi.org/10.1146/annurev-marine-010318-095251

Harris, P.M., 1979. Facies anatomy and diagenesis of a Bahamian ooid shoal. Sedimenta VII. Comparative Sedimentology Laboratory, University of Miami. https://doi.org/10.1002/embr.201338114

Harris, P.M., Purkis, S.J., Ellis, J., Swart, P.K., Reijmer, J.J.G., 2015. Mapping bathymetry and depositional facies on Great Bahama Bank. Sedimentology 62, 566–589. https://doi.org/10.1111/sed.12159

Heezen, B.C., Tharp, M., Ewing, M., 1959. The floors of the oceans: I. The North Atlantic, GSA Special Papers. Geological Society of America. https://doi.org/https://doi.org/10.1130/SPE65-p1

Higgins, J.A., Fischer, W.W., Schrag, D.P., 2009. Oxygenation of the ocean and sediments: Consequences for the seafloor carbonate factory. Earth Planet. Sci. Lett. 284, 25–33. https://doi.org/10.1016/j.epsl.2009.03.039

ICS, 2013. International Chronostratigraphic Chart [WWW Document]. URL www.stratigraphy.org/ICSchart/ChronostratChart2013-01.pdf

Keim, L., Schlager, W., 2001. Quantitative compositional analysis of a Triassic carbonate platform (Southern Alps. Italy). Sediment. Geol. 139, 261–283. https://doi.org/10.1016/S0037-0738(00)00163-9

Kelley, B.M., Lehrmann, D.J., Yu, M., Jost, A.B., Meyer, K.M., Lau, K. V., Altiner, D., LI, X., Minzoni, M., Schaal, E.K., Payne, J.L., 2020. Controls on carbonate platform architecture and reef recovery across the Palaeozoic to Mesozoic transition: A high-resolution analysis of the Great Bank of Guizhou. Sedimentology. https://doi.org/10.1111/SED.12741

Kelley, B.M., Lehrmann, D.J., Yu, M., Minzoni, M., Enos, P., Li, X., Lau, K.V., Payne, J.L., 2017. The Late Permian to Late Triassic Great Bank of Guizhou: An isolated carbonate platform in the Nanpanjiang Basin of Guizhou Province, China. Am. Assoc. Pet. Geol. Bull. 101. https://doi.org/10.1306/011817DIG17034

Kenter, J.A.M., Harris, P.M., Della Porta, G., 2005. Steep microbial boundstone-dominated platform margins - Examples and implications. Sediment. Geol. 178, 5–30. https://doi.org/10.1016/j.sedgeo.2004.12.033

Kerans, C., Playton, T., Phelps, R., Scott, S.Z., 2013. Ramp to rimmed shelf transition in the Guadalupian (Permian) of the Guadalupe Mountains, West Texas and New Mexico, in: Verwer, K., Playton, T.E., Harris, P.M. (Eds.), Deposits, Architecture, and Controls of Carbonate Margin, Slope and Basinal Settings. SEPM Special Publication 105, pp. 26–49. https://doi.org/10.2110/sepmsp.105.13

Kolodka, C., Vennin, E., Bourillot, R., Granjeon, D., Desaubliaux, G., 2015. Stratigraphic modelling of platform architecture and carbonate production: a Messinian case study (Sorbas Basin , SE Spain). Basin Res. 1–27. https://doi.org/10.1111/bre.12125

Lehrmann, D.J., 1999. Early Triassic calcimicrobial mounds and biostromes of the Nanpanjiang basin, south China. Geology 27, 359–362. https://doi.org/10.1130/0091-7613(1999)027<0359:ETCMAB>2.3.CO;2

Lehrmann, D.J., Chaikin, D.H., Enos, P., Minzoni, M., Payne, J.L., Yu, M., Goers, A., Wood, T., Richter, P., Kelley, B.M., Li, X., Qin, Y., Liu, L., Lu, G., 2015a. Patterns of basin fill in Triassic turbidites of the Nanpanjiang basin: Implications for regional tectonics and impacts on carbonate-platform evolution. Basin Res. 27, 587–612. https://doi.org/10.1111/bre.12090

Lehrmann, D.J., Donghong, P., Enos, P., Minzoni, M., Ellwood, B.B., Orchard, M.J., Jiyan, Z., Jiayong, W., Dillett, P., Koening, J., Steffen, K., Druke, D., Druke, J., Kessel, B., Newkirk, T., 2007. Impact of differential tectonic subsidence on isolated carbonate-platform evolution: Triassic of the Nanpanjiang Basin, south china. Am. Assoc. Pet. Geol. Bull. 91, 287–320. https://doi.org/10.1306/10160606065

Lehrmann, D.J., Minzoni, M., Enos, P., Kelleher, C., Stepchinski, L., Li, X., Payne, J.L., Yu, M., 2020. Giant sector-collapse structures (scalloped margins) of the Yangtze Platform and Great Bank of Guizhou, China: Implications for genesis of collapsed carbonate platform margin systems. Sedimentology. https://doi.org/10.1111/sed.12740

Lehrmann, D.J., Minzoni, M., Li, X., Yu, M., Payne, J.L., Kelley, B.M., Schaal, E.K., Enos, P., 2012. Lower Triassic oolites of the Nanpanjiang Basin, south China: Facies architecture, giant ooids, and diagenesis-implications for hydrocarbon reservoirs. Am. Assoc. Pet. Geol. Bull. 96. https://doi.org/10.1306/01231211148

Lehrmann, D.J., Stepchinski, L., Altiner, D., Orchard, M.J., Montgomery, P., Enos, P., Ellwood, B.B., Bowring, S.A., Ramezani, J., Wang, H., Wei, J., Yu, M., Griffiths, J.D., Minzoni, M., Schaal, E.K., Li, X., Meyer, K.M., Payne, J.L., 2015b. An integrated biostratigraphy (conodonts and foraminifers) and chronostratigraphy (paleomagnetic reversals, magnetic susceptibility, elemental chemistry, carbon isotopes and geochronology) for the Permian-Upper Triassic strata of Guandao section, Nanpanji. J. Asian Earth Sci. 108, 117–135. https://doi.org/10.1016/j.jseaes.2015.04.030

Lehrmann, D.J., Wei Jiayong, Enos, P., 1998. Controls on facies architecture of a large Triassic carbonate platform; the Great Bank of Guizhou, Nanpanjiang Basin, south China. J. Sediment. Res. 68, 311–326. https://doi.org/10.2110/jsr.68.311

Li, F., Gong, Q., Burne, R. V., Tang, H., Su, C., Zeng, K., Zhang, Y., Tan, X., 2019. Ooid factories operating under hothouse conditions in the earliest Triassic of South China. Glob. Planet. Change 172, 336–354. https://doi.org/10.1016/j.gloplacha.2018.10.012

Li, X., Yu, M., Lehrmann, D.J., Payne, J.L., Kelley, B.M., Minzoni, M., 2012. Factors controlling carbonate platform asymmetry: Preliminary results from the Great Bank of Guizhou, an isolated Permian-Triassic Platform in the Nanpanjiang Basin, south China. Palaeogeogr. Palaeoclimatol. Palaeoecol. 315–316, 158–171. https://doi.org/10.1016/j.palaeo.2011.11.023

Liechoscki de Paula Faria, D., Tadeu dos Reis, A., Gomes de Souza, O., 2017. Three-dimensional stratigraphic-sedimentological forward modeling of an Aptian carbonate reservoir deposited during the sag stage in the Santos basin, Brazil. Mar. Pet. Geol. 88, 676–695. https://doi.org/10.1016/j.marpetgeo.2017.09.013

Lukasik, J., Simo, J.A., 2008. Controls on carbonate platform and reef development. SEPM Special Publication 89. https://doi.org/10.2110/pec.08.89

Marangon, A., Gattolin, G., Della Porta, G., Preto, N., 2011. The Latemar: A flat-topped, steep fronted platform dominated by microbialites and synsedimentary cements. Sediment. Geol. 240, 97–114. https://doi.org/10.1016/j.sedgeo.2011.09.001

Marchionda, E., Deschamps, R., Cobianchi, M., Nader, F.H., Di Giulio, A., Morad, D.J., Al Darmaki, F., Ceriani, A., 2018. Field-scale depositional evolution of the Upper Jurassic Arab Formation (onshore Abu Dhabi, UAE). Mar. Pet. Geol. 89, 350–369. https://doi.org/10.1016/j.marpetgeo.2017.10.006

Merino-Tomé, Ó., Porta, G. Della, Kenter, J.A.M., Verwer, K., Harris, P.M., Adams, E.W., Playton, T., Corrochano, D., 2012. Sequence development in an isolated carbonate platform (Lower Jurassic, Djebel Bou Dahar, High Atlas, Morocco): Influence of tectonics, eustacy and carbonate production. Sedimentology 59, 118–155. https://doi.org/10.1111/j.1365-3091.2011.01232.x

Meyer, K.M., Yu, M., Jost, A.B., Kelley, B.M., Payne, J.L., 2011. δ13C evidence that high primary productivity delayed recovery from end-Permian mass extinction. Earth Planet. Sci. Lett. 302, 378–384. https://doi.org/10.1016/j.epsl.2010.12.033

Minzoni, M., Lehrmann, D.J., Payne, J., Enos, P., Yu, M., Wei, J., Kelley, B., Li, X., Schaal, E., Meyer, K., Montgomery, P., Goers, A., Wood, T., 2013. Triassic tank: Platform margin and slope architecture in space and time, Nanpanjiang Basin, south China, in: Verwer, K., Playton, T.E., Harris, P.M. (Mitch) (Eds.), Deposits, Architecture, and Controls of Carbonate Margin, Slope and Basinal Settings. SEPM Special Publication 105, pp. 84–113. https://doi.org/10.2110/sepmsp.105.10

Payne, J.L., Lehrmann, D.J., Christensen, S., Wei, J., Knoll, A.H., 2006. Environmental and biological controls on the initiation and growth of a Middle Triassic (Anisian) reef complex on the Great Bank of Guizhou, Guizhou Province, China. Palaios 21, 193–237. https://doi.org/10.2110/paIo.2005.P05-58e

Payne, J.L., Lehrmann, D.J., Wei, J., Orchard, M.J., Schrag, D.P., Knoll, A.H., 2004. Large perturbations of the carbon cycle during recovery from the End-Permian extinction. Science (80-.). 305, 506–509. https://doi.org/10.1126/science.1097023

Phelps, R.M., Kerans, C., Da-Gama, R.O.B.P., Jeremiah, J., Hull, D., Loucks, R.G., 2015. Response and recovery of the Comanche carbonate platform surrounding multiple Cretaceous oceanic anoxic events, northern Gulf of Mexico. Cretac. Res. 54, 117–144. https://doi.org/10.1016/j.cretres.2014.09.002

Pierre, A., Durlet, C., Razin, P., Chellai, E.H., 2010. Spatial and temporal distribution of ooids along a

Jurassic carbonate ramp: Amellago outcrop transect, High-Atlas, Morocco, in: Van Buchem, F.S.P., Gerdes, K.D., Esteban, M. (Eds.), Mesozoic and Cenozoic Carbonate Systems of the Mediterranean and the Middle East: Stratigraphic and Diagenetic Reference Models. Geological Society of London Special Publications 329, pp. 65–88. https://doi.org/10.1144/SP329.4

Playton, T.E., Kerans, C., 2018. Architecture and genesis of prograding deep boundstone margins and debris-dominated carbonate slopes: Examples from the Permian Capitan Formation, Southern Guadalupe Mountains, West Texas. Sediment. Geol. 370, 15–41. https://doi.org/10.1016/j.sedgeo.2017.12.021

Pomar, L., 2001. Ecological control of sedimentary accommodation: Evolution from a carbonate ramp to rimmed shelf, Upper Miocene, Balearic Islands. Palaeogeogr. Palaeoclimatol. Palaeoecol. 175, 249–272. https://doi.org/10.1016/S0031-0182(01)00375-3

Preto, N., Gianolla, P., Franceschi, M., Gattolin, G., Riva, A., 2017. Geometry and evolution of Triassic high-relief, isolated microbial platforms in the Dolomites, Italy: The Anisian Latemar and Carnian Sella platforms compared. Am. Assoc. Pet. Geol. Bull. 101, 475–483. https://doi.org/10.1306/011817DIG17026

Purkis, S.J., Rowlands, G.P., Kerr, J.M., 2015. Unravelling the influence of water depth and wave energy on the facies diversity of shelf carbonates. Sedimentology 62, 541–565. https://doi.org/10.1111/sed.12110

Rankey, E.C., Reeder, S.L., 2011. Holocene oolitic marine sand complexes of the Bahamas. J. Sediment. Res. 81, 97–117. https://doi.org/10.2110/jsr.2011.10

Reeder, S.L., Rankey, E.C., 2008. Interactions between tidal flows and ooid shoals, Northern Bahamas. J. Sediment. Res. 78, 175–186. https://doi.org/10.2110/jsr.2008.020

Reijmer, J.J.G., Swart, P.K., Bauch, T., Otto, R., Reuning, L., Roth, S., Zechel, S., 2009. A re-evaluation of facies on Great Bahama Bank I: New facies maps of Western Great Bahama Bank, in: Swart, P.K., Eberli, G.P., McKenzie, J.A., Jarvis, I., Stevens, T. (Eds.), Perspectives in Carbonate Geology: A Tribute to the Career of Robert Nathan Ginsburg. Blackwell Publishing Ltd, pp. 29–46. https://doi.org/10.1002/9781444312065.ch3

Richet, R., Borgomano, J., Adams, E.W., Masse, J.P., Viseur, S., 2011. Numerical outcrop geology applied to stratigraphical modeling of ancient carbonate platforms: The Lower Cretaceous Vercors carbonate platform (SE France), in: Martinsen, O.J., Pulham, A.J., Haughton, P.D.W., Sullivan, M.D. (Eds.), Outcrops Revitalized: Tools, Techniques and Applications. SEPM Concepts in Sedimentology and Paleontology No. 10, pp. 195–209. https://doi.org/10.2110/sepmcsp.10.195

Saura, E., Embry, J.C., Vergés, J., Hunt, D.W., Casciello, E., Homke, S., 2013. Growth fold controls on carbonate distribution in mixed foreland basins: Insights from the Amiran foreland basin (NW Zagros, Iran) and stratigraphic numerical modelling. Basin Res. 25, 149–171. https://doi.org/10.1111/j.1365-2117.2012.00552.x

Scheibner, C., Reijmer, J.J.G., 1999. Facies patterns within a Lower Jurassic upper slope to inner platform transect (Jbel Bou Dahar, Morocco). Facies 55–80. https://doi.org/10.1007/bf02537460

Schlager, W., 2005. Carbonate sedimentology and sequence stratigraphy. SEPM Concepts in Sedimentology and Paleontology No. 8, Tulsa.

Schlager, W., 2003. Benthic carbonate factories of the Phanerozoic. Int. J. Earth Sci. 92, 445–464. https://doi.org/10.1007/s00531-003-0327-x

Seard, C., Borgomano, J., Granjeon, D., Camoin, G., 2013. Impact of environmental parameters on coral reef development and drowning: Forward modelling of the last deglacial reefs from Tahiti (French Polynesia; IODP Expedition #310). Sedimentology 60, 1357–1388. https://doi.org/10.1111/sed.12030

Spencer, R.J., Demicco, R. V., 1989. Computer models of carbonate platform cycles driven by subsidence and eustacy. Geology 17, 165–168. https://doi.org/10.1130/0091-7613(1989)017<0165:CMOCPC>2.3.CO;2

Swart, P.K., Reijmer, J.J., Otto, R., P.K., 2009. A re-evaluation of facies on Great Bahama Bank II: Variations in the δ13C, δ18O and mineralogy of surface sediments, in: Swart, Peter K., Eberli, G.P., McKenzie, J.A., Jarvis, I., Stevens, T. (Eds.), Perspectives in Carbonate Geology: A Tribute to the Career of Robert Nathan Ginsburg. Blackwell Publishing Ltd, pp. 47–60. https://doi.org/10.1002/9781444312065

Tinker, S.W., 1998. Shelf-to-basin facies distributions and sequence stratigraphy of a steep-rimmed carbonate margin; Capitan depositional system, McKittrick Canyon, New Mexico and Texas. J. Sediment. Res. 68, 1146–1174. https://doi.org/10.2110/jsr.68.1146

Van Der Kooij, B., Immenhauser, A., Steuber, T., Bahamonde Rionda, J.R., Meríno Tomé, O., 2010. Controlling factors of volumetrically important marine carbonate cementation in deep slope settings. Sedimentology 57, 1491–1525. https://doi.org/10.1111/j.1365-3091.2010.01153.x

Verwer, K., Merino-Tome, O., Kenter, J. a. M., Della Porta, G., 2009. Evolution of a high-relief carbonate platform slope using 3D digital outcrop models: Lower Jurassic Djebel Bou Dahar, High Atlas, Morocco. J. Sediment. Res. 79, 416–439. https://doi.org/10.2110/jsr.2009.045

Verwer, K., Playton, T.E., Harris, P.M. (Mitch), 2013. Deposits, architecture, and controls of carbonate margin, slope, and basinal settings. SEPM Special Publication 105. https://doi.org/10.2110/sepmsp.105.12

Warrlich, G., Bosence, D., Waltham, D., Wood, C., Boylan, A., Badenas, B., 2008. 3D stratigraphic forward modelling for analysis and prediction of carbonate platform stratigraphies in exploration and production. Mar. Pet. Geol. 25, 35–58. https://doi.org/10.1016/j.marpetgeo.2007.04.005

Warrlich, G.M.D., Waltham, D.A., Bosence, D.W.J., 2002. Quantifying the sequence stratigraphy and drowning mechanisms of atolls using a new 3-D forward stratigraphic modelling program (CARBONATE 3D). Basin Res. 14, 379–400. https://doi.org/10.1046/j.1365-2117.2002.00181.x

Williams, H.D., Burgess, P.M., Wright, V.P., Della Porta, G., Granjeon, D., 2011. Investigating carbonate platform types: Multiple controls and a continuum of geometries. J. Sediment. Res. 81, 18–37. https://doi.org/10.2110/jsr.2011.6

Wilson, P.A., Roberts, H.H., 1995. Density cascading: Off-shelf sediment transport, evidence and implications, Bahamas Banks. J. Sediment. Res. A65, 45–56. https://doi.org/10.1306/D426801D-2B26-11D7-8648000102C1865D

Wilson, P.A., Roberts, H.H., 1992. Carbonate-periplatforrn sedimentation by density flows: A mechanism for rapid off-bank and vertical transport of shallow-water fines. Geology 20, 713–716. https://doi.org/10.1130/0091-7613(1993)021<0667:CPSBDF>2.3.CO;2

Woods, A.D., Bottjer, D.J., Mutti, M., Morrison, J., 1999. Lower Triassic large sea-floor carbonate cements: Their origin and a mechanism for the prolonged biotic recovery from the end-Permian mass extinction. Geology 27, 645–648. https://doi.org/10.1130/0091-7613(1999)027<0645:LTLSFC>2.3.CO;2

Yang, W., Lehrmann, D.J., 2003. Milankovitch climatic signals in Lower Triassic (Olenekian) peritidal carbonate successions, Nanpanjiang Basin, South China. Palaeogeogr. Palaeoclimatol. Palaeoecol. 201, 283–306. https://doi.org/10.1016/S0031-0182(03)00614-X

Highlight:

- High carbonate saturation can promote a ramp to steep-sloped platform transition
- Carbonate platform growth is limited by production-capacity and transport-capacity
- Carbonate platform geometry is more sensitive to transport than sediment production

Declaration of interests

☒ The authors declare that they have no known competing financial interests or personal relationships that could have appeared to influence the work reported in this paper.

☐The authors declare the following financial interests/personal relationships which may be considered as potential competing interests: